The influence of warm winters on biospheric CO_2 determined from a novel application of atmospheric measurements.

Student no: 100223296

Dieu Anh Tran

Word Count: 8692

Thesis presented in part-fulfilment of the degree of Master of Science in accordance with the regulations of the University of East Anglia

School of Environmental Sciences

University of East Anglia

Norwich

NR4 7TJ

Acknowledgements

Many thanks to my supervisor Andrew Manning for his insight, guidance and feedback throughout this project. Thank you also to Penelope Pickers for her guidance in the conception of this project, valuable comments and providing the clean-up meteorological data. Finally, thank you to Leigh Fleming for providing me the O_2 and CO_2 data.

Abstract – About one-third of the world's anthropogenic emissions is offset by the global terrestrial carbon sink, but the strength of this sink is highly sensitive to anomalously high temperature periods. This study used complementary in-situ Atmospheric Potential Oxygen data and random forest machine learning to investigate the impact of the anomalously warm-winter-to-spring transition in 2015/16 and 2019/20 on the biospheric component of the total CO_2 variation at a mid-latitude study site – Weybourne Atmospheric Observatory, UK. For the 2015/16 and 2019/20 winters, there were positive anomalies of 1.52 ppm and 1.40 ppm respectively in the biospheric CO_2 concentration (relative to the 2011-2019 mean) suggesting potential higher respiratory release of CO_2 with increasing temperature. The increase in ecosystem respiration from the 2019/20 warm winter was partly compensated by an increase in photosynthesis during the following warm spring resulting in a larger seasonal amplitude compared to the mean and nearly neutral effects on the annual net CO_2. Notwithstanding, the CO_2 transition phase from winter to spring was slower in 2015/16 compared to the 2011-2019 mean, suggesting a delay in the growing season, with either continued CO_2 release by respiration from the warm winter months or a reduction in photosynthetic uptake driven by a cold snap and limited sunlight condition in the subsequent 2016 spring.

Table of Contents

1. Introduction

1.1. The global carbon cycle

The global carbon cycle is made up of carbon exchanges within and between four main reservoirs: the atmosphere, land, oceans, and fossil fuels (Figure 1.1) (e.g. IPCC AR4, 2014). Carbon dioxide (CO_2) fluxes between these reservoirs are stimulated by a variety of natural and anthropogenic processes (Sarmiento et al., 2010). Anthropogenic processes including burning fossil fuels and deforestation, add a large positive net flux to the atmosphere (Ciais et al., 2013). This source represented 9.80 Gt C yr^{-1} during the 2010s and is also considered to be the main cause of significantly large increases in the atmospheric CO_2 since 1900 (Lollar, 2014). Of the carbon released into the atmosphere through fossil fuel combustion approximately 56% has remained there, with the other 44% being taken up by natural processes, primarily terrestrial and oceanic photosynthetic absorption of CO_2 (the ocean has the highest natural flux of 2.40 Gt C yr^{-1} and the terrestrial biosphere has slightly smaller net sink of 0.70 Gt C yr^{-1}) (Sarmiento et al., 2010). The remaining anthropogenic CO_2 in the atmosphere has resulted in a greenhouse effect causing the global climate to experience unequivocal rates of warming (IPCC, 2014). Based on different emission scenarios, the global mean surface temperature is projected to increase between 0.30 and 4.80°C by the end of this century (IPCC, 2018).

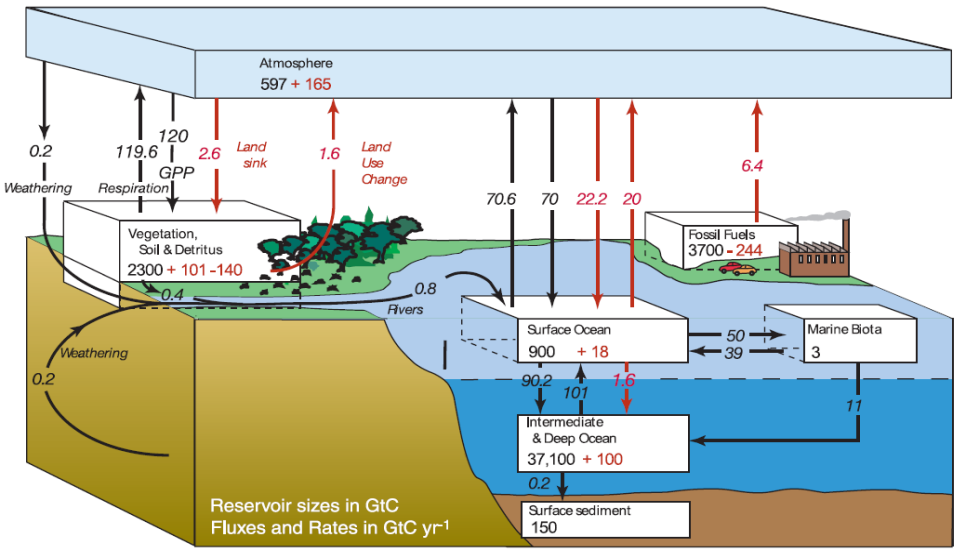

Figure 1.1 The global carbon cycle and the relative fluxes of carbon between the reservoirs (Source: IPCC AR4, 2014). Numbers inside the boxes is reservoir size (in Gt C). Natural and anthropogenic fluxes (in Gt C yr^{-1}) are indicated by black arrows and red arrows respectively.

1.2. Terrestrial carbon balance

The difference between carbon absorption by photosynthesis and release by respiration and other disturbances such as fire and deforestation is the net flux of carbon between the atmosphere and the terrestrial biosphere. All these processes have resulted in a net sink of atmospheric CO_2 by terrestrial ecosystems over the last three decades (Le Quéré et al., 2016). The global terrestrial biosphere absorbs ~30% of the anthropogenic CO_2 released every year, slowing global warming by mitigating the growth of CO_2 in the atmosphere (Le Quéré et al., 2016). The terrestrial biosphere is, in addition, one of the most significant contributors to the annual variability of the atmospheric CO_2 (Reichstein et al., 2013). However, its connection to climate variability is still poorly understood, resulting in interannual residuals varying between ± 2.00 Pg C yr^{-1} when closing the global carbon balance (Reichstein et al., 2013). Part of this residual variation could potentially be explained by the extreme changes in some climate parameters including precipitation, temperature and radiation regimes (IPCC, 2014). Extreme changes in those parameters could alter the terrestrial carbon balance more easily than gradual climate change owing to typically greater impact strengths in shorter times (Niu et al., 2014). Temperature extremes, for example, may have a direct and simultaneous effect on photosynthesis and respiration (Figure 1.2). Very high temperatures have various concurrent direct influences on plant physiological functions, ranging from disturbances in enzyme activity affecting photosynthesis and respiration rates to changes in plant growth (Lobell et al., 2012; Niu et al., 2014). Similarly, extremely low temperatures could impact plant characteristics and increase plant mortality from frost damage (Larcher, 2003). Meanwhile, climate models predict global strengthening of stronger or longer-lasting extreme high temperature periods in the global warming scenario (e.g. Fisher & Knutti, 2014). Therefore, it is critical to gain a better understanding of the influence of anomalous high-temperature periods on the terrestrial carbon balance to better project changes under future heat extremes associated with climate change.

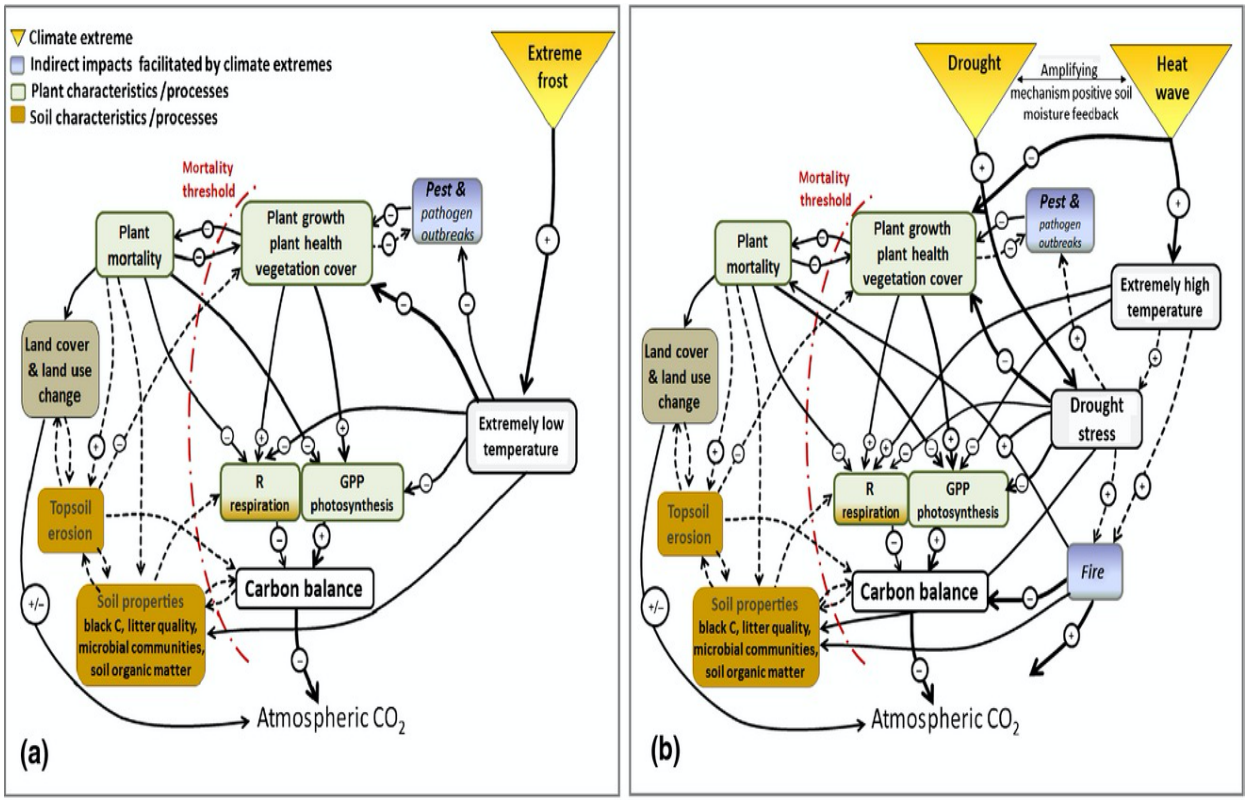

Figure 1.2. The processes and dynamics underpinning the impacts of (a) extremely cold temperature and (b) extremely high temperature on the carbon cycle. Positive/enhancing impacts are indicated by a '+' symbol, while negative/reducing impacts are indicated by a '-' sign; (in)direct impacts are shown in (dashed) arrows; impact/relationship significance is indicated by arrow thickness (high = thick, low = thin) (Source: Reichstein et al., 2013).

1.3. Literature review

Direct and concurrent impacts of anomalous temperatures on plant physiology could influence photosynthesis and respiration processes and hence alter the terrestrial carbon sink. This section evaluates the literature regarding the influences of different past extreme high-temperature events on the net terrestrial carbon sink.

a. Heatwaves and droughts

Although droughts and heatwaves are both weather extremes on their own, they cannot be considered as separate events since droughts are typically the direct consequences of high-temperature extremes leading to high evaporative demand on ecosystems (Larcher, 2003). Heatwaves and droughts could cause modifications in plant characteristics such as decrease in leaf area index, changes in the root–shoot ratio (Mueller & Seneviratne, 2012; Bréda et al.,

2006) or in plant physiological processes including closing stomata to reduce water loss and lowering the activity and concentrations of photosynthetic enzymes (Lawlor, 1995; Keenan et al., 2010). Droughts, therefore, could decrease CO_2 assimilation rates (the process by which CO_2 from the atmosphere is converted to organic compounds through plant photosynthesis) and reduce carbon sink strength (Palacio et al., 2014). Usually, the direct effects of droughts on plant photosynthesis are greater than those on plant respiration (Fig. 1.2b) (Atkin and Macherel, 2009).

The 2003 European heatwave is an example of the impact of an anomalous high-temperature period coupled with drought on the carbon fluxes. Ciais et al. (2005) used satellite CO_2 remote sensing and atmospheric inverse modelling (which relies on atmospheric measurements of greenhouse gases (GHGs), and an atmospheric transport model simulating the transport of the gases from theirs emissions source to the location of the measurement) to infer GHG fluxes at the Earth surface in order to assess continental-scale changes in Gross Primary Production (GPP) – the total amount of carbon absorbed into an ecosystem through terrestrial photosynthesis (See Appendix A – Figure A1). They estimated a 30% decrease in GPP (See Appendix A – Figure A2), as a consequence of heat stress and decrease in soil moisture, which led to plant stomatal closure to minimize transpiration resulting in lower photosynthetic rates. This explanation was also supported by other studies (e.g. Reichstein et al., 2007; Granier et al., 2007). Similarly, there was a decrease in terrestrial ecosystem respiration instead of an increase coupled with the high temperatures because water deficit, again, could also lower auto- and heterotrophic respiration. The decrease in GPP was not entirely offset by the decrease in respiration leading to a net source of CO_2 from the terrestrial biosphere to the atmosphere in 2003.

Thompson et al. (2020) also used an atmospheric inversion model to quantify the effect of the 2018 European drought on Net Ecosystem Exchange (NEE) which is the net CO_2 exchange with the atmosphere, that is, the CO_2 flux from the ecosystem to the atmosphere. They found that the NEE in 2018 was slightly more positive by 0.09 ± 0.06 Pg C yr^{-1} than the last 10-year mean of -0.08 ± 0.17 Pg C yr^{-1} indicating a reduction in the terrestrial CO_2 uptake (See Appendix A – Figure A3). These positive NEE anomalies agreed spatially and temporally with negative anomalies in soil water. Similarly, Ramonet et al. (2020) used observational CO_2 data from 48 European stations to investigate the influence of the 2018 heatwave and drought on the amplitude of the CO_2 seasonal cycles, and found that the usual summer minimum in CO_2 due to terrestrial carbon sink was 1.40 ppm higher for the 10 stations located

in Northern Europe where is most affected by the heatwave (See Appendix A – Figure A4), suggesting a reduction in summer carbon uptake as a result of the drought.

Wolf et al. (2016) combined satellite remote sensing and atmospheric inverse modelling to estimate the effects of 2012 warm spring and summer drought on the Net Ecosystem Production (NEP) (which is equal to GPP minus the amount of carbon losses in ecosystem respiration). They consistently found that there was a big reduction in NEP of -32.00 ± 18.00 g C indicating a decrease in net CO_2 uptake during the severe summer drought (See Appendix A – Figure A5). However, this reduction was compensated by an increase in carbon uptake in the previous warm spring. The warmer temperatures during the growing season could have enhanced plant growth and vegetation activity leading to increasing net carbon uptake. Their findings suggest that the detrimental influences of a prolonged summer drought on the terrestrial carbon balance could be naturally mitigated by warmer springs increasing the spring carbon sink.

b. Warm winters

Warm winters are one of the anomalous high-temperature events that could have a significant influence on the terrestrial carbon balance. Plant and soil respiration are one of the key processes during the winter months that are responsible for the variations in atmospheric CO_2. Winters with higher temperatures are expected to increase both microbial and plant respiration enhancing the respiratory release of CO_2 (Buras et al, 2020) and thereby weakening the annual net terrestrial carbon sink.

Liu et al. (2019) investigated the impacts of the 2016 anomalously warm winter to spring transition period on the net CO_2 seasonal cycle across Alaska using ensemble atmospheric inverse model simulations and satellite observations. During the warm winter, they found that respiration was enhanced more than photosynthesis, leading to lower CO_2 uptake compared to the 2010-2014 mean. However, the warm-winter-induced higher respiration was compensated by an increase in photosynthesis during the subsequent warm spring, leading to closely neutral effects on the annual net CO_2 balance (See Appendix A – Figure A6). Their findings indicate that air temperature has a significant impact on net CO_2 balance at high latitudes during winter and spring.

In another study, Commane et al. (2017) examined a 40-year dataset of hourly observational atmospheric CO_2 from the land sector at Barrow, Alaska. Their results suggest that over the last 41 years, CO_2 concentration during October to January period, which is primarily from ecosystem respiration, has increased by ~73% ± 10.8% from carbon-rich soils

on the Alaska North Slope (See Appendix A – Figure A7), in agreement with rising winter temperatures associated with global warming.

1.4. Motivation and objectives

The review above acknowledges the potential effects of anomalously high-temperature events on the terrestrial carbon sink. Heatwaves and droughts in the summer could significantly decrease plant photosynthetic rates and hence weaken the net carbon sink. Warmer temperatures in the spring, on the other hand, extend the duration of plant activity, favour plant growth, and therefore increase net carbon absorption. Whereas warmer winters could increase the atmospheric CO_2 concentration through increased plant respiration. Additionally, the studies mentioned above also highlight the use of inverse modelling as a common method to quantify regional terrestrial ecosystem CO_2 fluxes.

While prolonged heatwave events are becoming more frequent, cold snaps are getting shorter and less likely, therefore exacerbating the occurrence of warm winters (Frank et al., 2015). If warm winters occur at an increasing rate as predicted, the amount of winter respiratory release of CO_2 could be significantly enhanced (Natali et al., 2011; Webb et al., 2016; Zona et al., 2016). This could potentially shift northern hemisphere ecosystems from net carbon sinks to net carbon sources, thus strengthening a positive carbon-climate feedback that exacerbates the impacts of climate change (e.g. Huang et al., 2017; Koven et al., 2011; Schaefer et al., 2014).

Despite the potential impacts of warm winters on the carbon balance, however, only a few studies investigated this type of high-temperature anomaly. The studies of Liu et al. (2019) and Commane et al. (2017) discussed above are the only two among a few that investigated this and they both focus on the response of high-latitude ecosystems which are more sensitive to soil thaw releasing CO_2 with increasing winter temperatures. My study builds on the reviewed literature but focuses on the response of the terrestrial carbon balance that is associated with anomalous warm-winter-to-spring transitions at a mid-latitude regional study site. Additionally, instead of using the common model-based method to quantify terrestrial biospheric CO_2 ($bioCO_2$) as in most studies discussed above, this project will use a novel observation-based method using Atmospheric Potential Oxygen.

Study objectives:

a) Investigate whether the bioCO_2 concentration of two warm winters (2015/16 and 2019/20) is higher compared to (1) their 'counterfactual cases' (i.e. hypothetical 2015/16 and 2019/20 winters without the warming); and (2) other normal winters.
b) Investigate whether the amplitude of the bioCO_2 diurnal cycle during 2015/16 and 2019/20 winters is smaller than that during other normal winters.
c) Investigate (1) which meteorological variable (temperature, irradiation, relative humidity, surface pressure, wind speed and wind direction) is the most important in regulating bioCO_2 and (2) whether there are any trends between the bioCO_2 and those meteorological parameters in the two counterfactual cases.

2. Study system and justifications

2.1. Study site

All atmospheric and meteorological measurements were obtained from Weybourne Atmospheric Observatory (WAO). WAO is located on the north Norfolk coast of the UK (sample air inlet is 10 m above ground level and 20 m above sea level), approximately 35 km north west of Norwich, 170 km north east of London and 200 km east of Birmingham (Figure 2.1). It is part of the European Union's Integrated Carbon Observation System and the World Meteorological Organization's Global Atmosphere Watch programme. It has high-precision, high-accuracy, continuous and long range measurements of numerous species of atmospheric gases (including GHGs, isotopes, and reactive gases) at fine temporal scale. The large range and quantity of continuous measurement data being collected at WAO presents a unique opportunity to accurately calculate APO in order to separate terrestrial and anthropogenic CO_2 signals.

Figure 2.1. Location of WAO on the North Norfolk coast, UK (Source: Google Maps).

2.2. Study periods

Both 2015/16 and 2019/20 winters experienced record high temperatures all around the northern hemisphere. Subsequently, this study focuses on the variability of the bioCO_2 concentration during these two winter-spring transition periods (August to the end of May).

a. 2015/16

2015 was the warmest year on record globally, with the northern hemisphere 0.76°C above the 1961–1990 mean (WMO, 2016). 2015/16 was the third mildest winter (December to February) overall for the UK at 5.50°C, behind only 2007 (5.60°C) and 1989 (5.80°C). Temperatures were widely 2.20°C above the 1981–2010 climatology across central and southern England (McCarthy et al., 2016). 2015/16 Three-month winter (December to February) mean temperature at WAO was 1.90°C significantly above the 2011-2019 mean (Figure 2.2).

The driver of this anomalously warm winter is suggested to be the global 2015/2016 El Niño (from May 2015 to March 2016), which was one of the strongest El Niño events on record (Scaife et al., 2017). Fereday et al. (2008) demonstrated a weak but significant correlation between El Niño-like patterns of sea surface temperatures in the tropical Pacific with the warm winter (November to February) occurrence in the North Atlantic region as observed in the UK.

The subsequent 2016 mean spring temperatures in the Southern areas were slightly cooler than mean in March (UK anomaly -0.50°C), and further cooler in April (-1.20°C) whereas May (+0.90°C) was a warm month for the region (National Climate Information Centre, 2016). High-pressure systems established during April and May brought plenty of fine, settled weather, particularly in the southeast. At WAO, the temperatures in April and May were 1.80 and 0.20°C lower than the 2011-2019 mean (Figure 2.2).

b. 2019/20

Temperatures were exceptionally high around the world during the 2019/20 winter. It was the second warmest winter (December to February) ever recorded for the global average, and the warmest for land areas only (Tandon and Schultz, 2020). Across the entirety of the UK, the mean winter temperature was 1.00°C or higher than the 1981-2010 baseline (Tandon and Schultz, 2020). At WAO, the three-month winter (DJF) mean temperature was significantly above the 2011-2019 mean by 2.02°C (Figure 2.2).

Additionally, the UK was struck by three storms in succession in February 2020, resulting in prolonged periods of heavy rainfall and extensive floods throughout most of

England and Wales (Tandon and Schultz, 2020). Unlike the earlier record-holding year of 2015/16, this warm winter was not boosted by an El Niño event but by a Foehn effect which is a type of warm, dry and down-slope wind that occurs in the lee side of a mountain range (Tandon and Schultz, 2020). This phenomenon could be expected during a very mild south-westerly airflow from the North Atlantic (Kendon et al., 2020).

High-pressure systems dominated much of the 2020 spring, resulting in sunny and dry weather conditions (Tandon and Schultz, 2020), and was the sunniest spring recorded in the UK since 1929. At WAO, the temperatures in April and May were 1.70 and 1.80°C higher than the 2011-2019 mean.

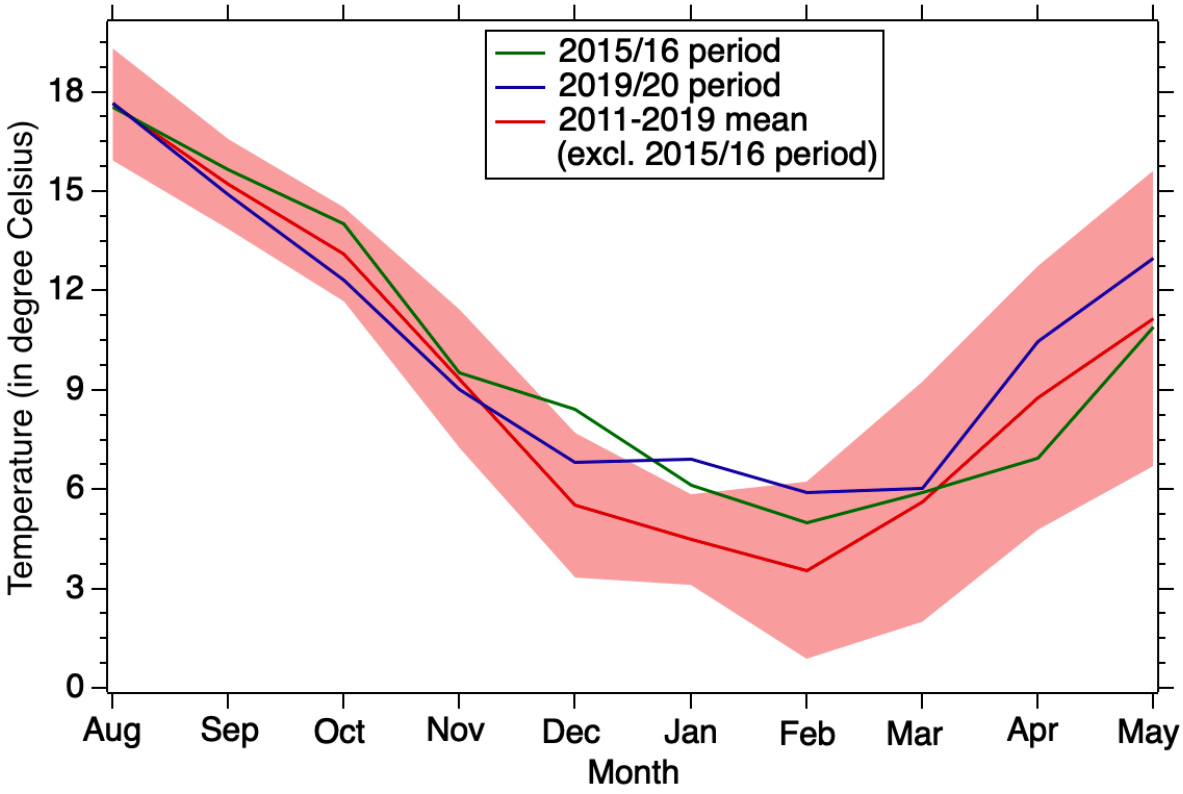

Figure 2.2. Monthly temperature (in °C) measured at WAO. The 2015/16 period is shown in green, 2019/20 in blue and the baseline mean (01/08/2011-31/07/2019 excluding 01/08/2015-31/07/2016 as this period includes the 2015/16 warm winter) in red. The red shading is two standard deviation (2σ) away from the monthly mean value.

2.3. Quantifying bioCO_2 signals using Atmospheric Potential Oxygen

Having an accurate method for determining bioCO_2 signals plays an important role in achieving the key objectives of this study. As seen in the literature review, one common method

to quantify bioCO_2 signals is inverse modelling which relies heavily on the atmospheric transport model employed. The transport model first estimates contributions of other components within the global carbon cycle to the variability of the observed CO_2, namely anthropogenic emissions, atmospheric transport, and air-ocean CO_2 fluxes (Regnier et al., 2013; Gurney et al., 2004; Gurney et al., 2008; Peylin et al., 2013). These other components are then subtracted from the observed atmospheric CO_2 to calculate the inverted biospheric signals (Ballantyne et al., 2015). Hence, any error in the calculations of the fluxes in these components could result in biases in the inverted bioCO_2 signals (Goeckede et al., 2010b).

The main bias in estimating regional-scale bioCO_2 signals using this model-based approach is associated with the uncertainties in estimating the anthropogenic component using atmospheric transport models. These models use bottom-up anthropogenic emission inventories to compute the regional anthropogenic contribution (Oney et al, 2017). This inventory method calculates GHG emissions using emission factors which are vulnerable to large uncertainties and biases because they are based on the raw materials used for various economic activities, rather than the actual emissions that are generated by such economic activities (Pickers, 2016). To prevent some of the drawbacks of using the model-based method to estimate anthropogenic CO_2 which could then lead to large uncertainty in estimations of biospheric signals, an observation-based estimation of the anthropogenic component can be applied (Oney et al, 2017). In this study, Atmospheric Potential Oxygen will be used as a tracer for anthropogenic CO_2 source.

When a terrestrial ecosystem removes 1 mole of CO_2 from the atmosphere, it also releases 1.1 moles of oxygen (O_2) (Severinghaus, 1995). CO_2 and O_2 are exactly anticorrelated (with a global average molar ratio of 1.1) for all terrestrial biosphere processes (photosynthesis, respiration and combustion) (See Appendix A – Figure A9). This relationship defines a quantity known as Atmospheric Potential Oxygen (APO) ($APO = O_2 + 1.1 \times CO_2$) (Stephens et al., 2000). Since O_2 and CO_2 variations from terrestrial biosphere processes are anti-correlated (Figure 2.3), they will cancel each other out in APO (Stephens et al., 2000). APO is, therefore, conservative with respect to all terrestrial biospheric processes. Variations in APO data therefore not only indicate variations in the exchange of O_2 and CO_2 of the ocean-atmosphere system on seasonal and longer timescales, but also variations in fossil fuel emissions on both shorter and longer timescales (Pickers, 2020), since fossil fuel emissions have O_2:CO_2 molar ratios different from that of the terrestrial biosphere. The applicability of APO as a tracer for anthropogenic CO_2 has been shown to be more precise, more accurate, less costly than other existing methods (e.g. using CO) and can be applied independently from

radiocarbon measurements (Pickers, 2016; Pickers et al., 2020). All these qualities make this APO-based method an excellent approach to derive the anthropogenic CO_2, from which the bioCO_2 signal and its uncertainty can easily be estimated.

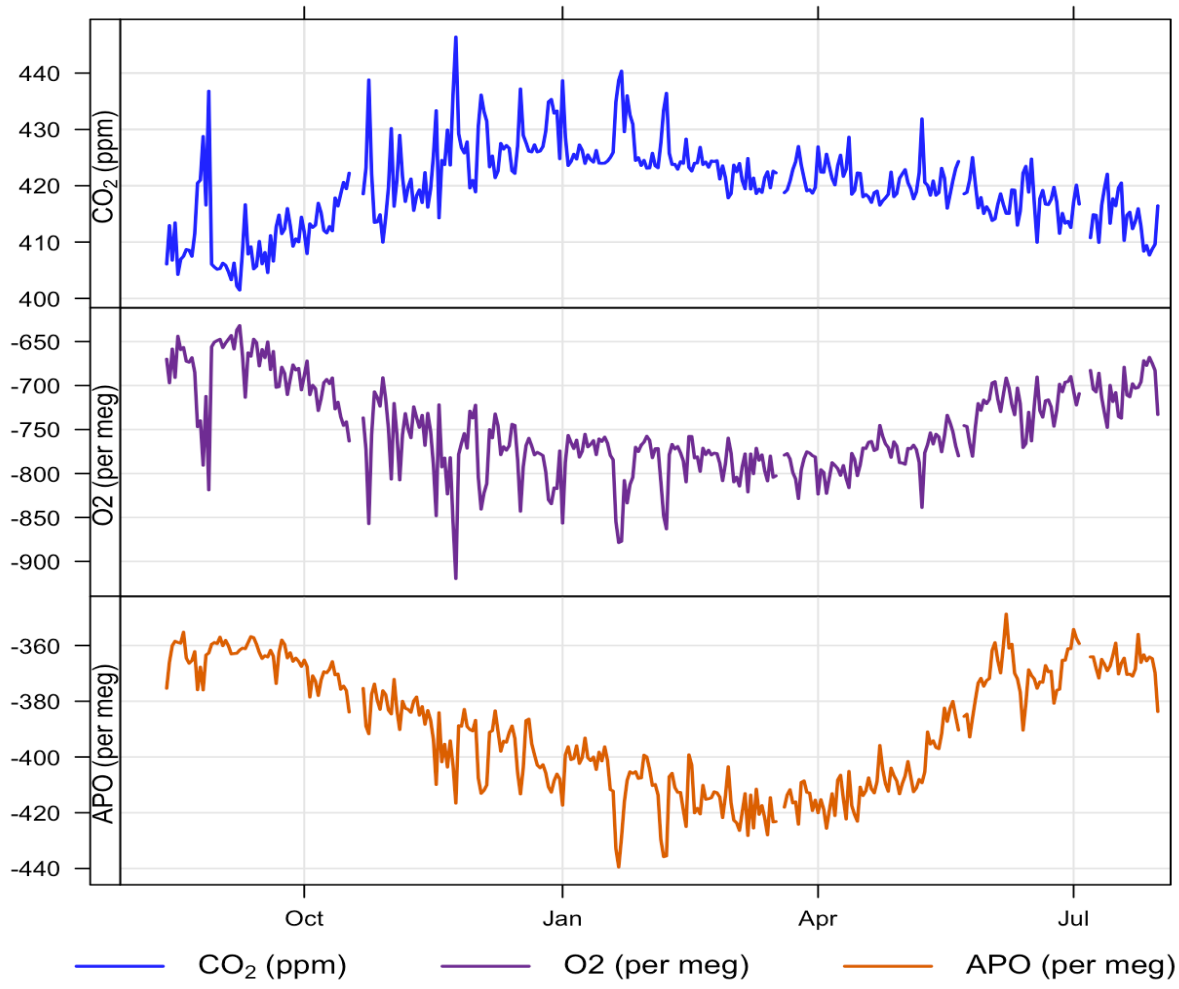

Figure 2.3. Daily timeseries of atmospheric CO_2 in ppm (top panel), O_2 in 'per meg' units (middle panel), and APO in 'per meg' units (bottom panel) from WAO between 01/08/2019–31/07/2020. Each panel shows seasonality that is driven mostly by terrestrial biospheric processes (CO_2 and O_2) and oceanic processes (O_2 and APO). Shorter term variability in APO is driven by diurnal processes, changes in meteorological conditions, synoptic-scale variability, and fossil fuel CO_2 emissions.

2.4. Using random forest to create counterfactual cases

To investigate how bioCO_2 concentrations of the two winters 2015/16 and 2019/20 would vary without the warming, random forest (RF), which is an ensemble decision tree machine learning (ML) method (Breiman, 2001), will be used to create their 'counterfactual cases'. The decision tree splits several observations using a binary algorithm into two

homologous groups, known as branches, repeating the process until the tree is fully grown (or till the branch node purity is achieved) (Tong et al., 2003). This kind of algorithm is known to be 'greedy' (Biau et al., 2008) and could lead to very deep trees where the terminal splits only evaluating two observations (Breiman, 2001). As a result, this type of model normally deals very poorly with new data which was not used to train the model (Tong et al., 2003). The decision tree method, therefore, is very sensitive to overfitting (Kotsiantis, 2013). RF overcomes this problem by using a technique known as bagging – a process that randomly samples observation and influencing variables with replacement to create several individual decision trees from a training dataset (Friedman et al., 2001). All the trees' outputs are then combined for prediction (Figure 2.4) (Caruana and Niculescu-Mizil, 2006).

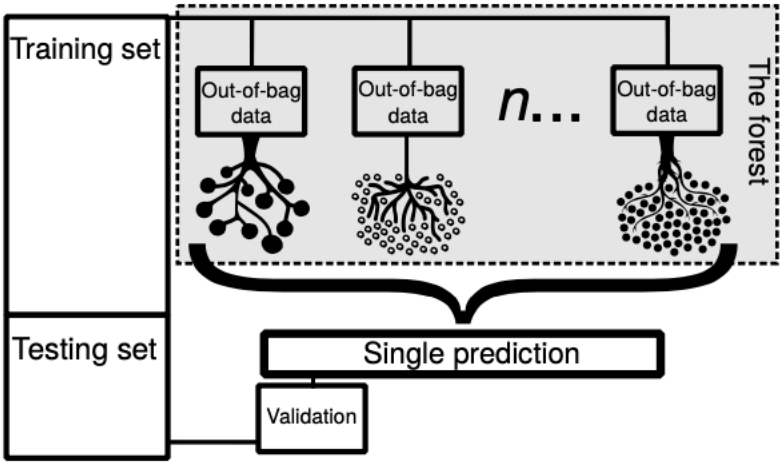

Figure 2.4. Conceptual diagram of an RF model (Source: Grange et al., 2018). From the training series, multiple out-of-bag samples (a set which results from the bagging process) are created and multiple decision trees are grown from those samples. All the trees' outputs are then combined for one prediction. The test set which is withdrawn from the training phase will then be used to evaluate the model prediction

.

RF is one of the few ML methods whose training process can be inspected and interpreted (Kotsiantis, 2013). RF models can produce partial dependence plots which demonstrate the relationships between observation and influencing variables, and a variable importance graph showing the importance of each influencing variable in predicting the output (Friedman et al., 2001; Jones and Linder, 2015). RF can be used in unsupervised regression and is known to be simpler to operate than other decision tree techniques (Immitzer et al.,

2012). The combination of these attributes has made RF a perfect ML technique to create counterfactual predictions and obtain objective 3 for this project.

3. Method

3.1. Data

Atmospheric O_2 at WAO is measured with a Sable Systems International Inc. 'Oxzilla II' electrochemical fuel cell analyser and CO_2 is measured with a Siemens Corporation 'Ultramat 6E' non-dispersive infrared analyser. Both gases are measured every two minutes. Atmospheric CO_2 measurements are reported in ppm while O_2 measurements are reported as (O_2/N2) ratios in per meg units since O_2 is not a trace gas and its mole fraction can be altered by changes in the concentration of other gases, such as CO_2 (Pickers et al., 2020).

There is a continuing increase (decrease) in the atmospheric CO_2 (O_2) data caused by anthropogenic CO_2 emissions (atmospheric O_2 is declining as combustion consumes O_2). To eliminate this long-term increasing trend in CO_2 (decreasing trend in O_2) data the slope of the CO_2 (or O_2) concentration-time linear regression was subtracted from CO_2 (or O_2) data (See Appendix C for more details on detrending the data).

APO is a tracer invariant to terrestrial biosphere-atmosphere exchange (See Appendix A – Figure A8) and was calculated from measurements of atmospheric O_2 and CO_2 using the aforementioned R script:

$$APO = O_2 + \frac{-1.1}{0.2095} \times (CO_2 - 350) \qquad \textbf{Equation 1}$$

where -1.1 is an estimate of the mean O_2:CO_2 ratio for land photosynthesis and respiration, 0.2095 is the mole fraction of O_2 molecules in dry air, and 350 is an arbitrary reference (Pickers, 2016). Multiplying CO_2 by -1.1 and dividing by 0.2095 converts the CO_2 data from ppm to per meg units (Lueker et al., 2003).

The fossil fuel (anthropogenic) component of total atmospheric CO_2 concentration ($ffCO_2$) in ppm at WAO was calculated using hourly APO data:

$$ffCO_2[APO] = \frac{APO - APO_{bg}}{R_{APO}} \qquad \textbf{Equation 2}$$

where APO is the atmospheric value calculated from Equation 1, APO_{bg} is the hourly APO 'background' or baseline values (i.e. values that are representative of the well-mixed troposphere of the wider region) with 1-week smoothing, which were determined using a statistical baseline fitting method using the 'rfbaseline' function from the 'IDPmisc' package in R, and R_{APO} is the APO:CO_2 combustion ration for fossil fuel emissions at WAO. The APO:CO_2 emission ratio used in this study was chosen to be a fixed ratio of -0.30 mol mol^{-1} as in Pickers et al. (2020).

The hourly estimates of bioCO_2, i.e. the atmospheric CO_2 variability driven by regional CO_2 fluxes from the terrestrial biosphere via photosynthesis and respiration, in units of ppm were produced from:

$$bioCO_2[APO] = CO_2 - ffCO_2[APO] \qquad \textbf{Equation 3}$$

where CO_2 is the total atmospheric CO_2 concentration in ppm and $ffCO_2[APO]$ is calculated from Equation 2.

One of the main assumptions of this study is that bioCO_2 signals are all terrestrial signals. BioCO_2 could also be hugely influenced by the ocean. However it takes about a year for ocean-atmospheric carbon to reach equilibrium. Therefore oceanic influences on bioCO_2 in the monthly signals observed in this study are considered to be negligible.

To address how the 2015/16 and 2019/20 warm winters affected the seasonal carbon cycle at WAO, the bioCO_2 concentration of the warm winter periods (01/08/2015-31/07/2016 and 01/08/2019-31/07/2020) were compared to the 01/08/2011-31/07/2019 baseline mean (excluding the 01/08/2013-31/07/2014 period due to large gaps in APO data). The data of each period was normalised by subtracting the 9-month mean value from the bioCO_2[APO] data (negative values indicate net CO_2 uptake by the regional terrestrial biosphere and vice versa).

The amplitudes of the CO_2 diurnal cycle were analysed by calculating the difference of the mean night-time concentrations (01:00-05:00 UTC) compared to the mean daytime values (11:00-15:00 UTC) for each day.

3.2. Modelling

A random forest (RF) model was trained for the period from 01/01/2011 to 31/07/2019 excluding the 01/08/2013-31/07/2014 period (big gaps in APO data) and the 01/08/2015-31/05/2016 period (predicted period is omitted from the training model). The 'rmweather' Package in R was used for this process. Similar to Grange et al. (2018), in my study, the number of trees for the RF models was fixed at 300, the minimal node size was five, and the number of variable split at each node was the default for regression mode: the rounded down the square root of the number of independent variables which in this example was three. All trees used the same influencing variables to predict daily bioCO_2. The influencing variables were: hourly meteorological observations (wind speed, wind direction, air temperature, relative humidity and atmospheric pressure), which were measured at WAO; temporal factors (day of the year, day of the week, hour of the day); and hourly 24-hour long HYSPLIT (Hybrid Single Particle Lagrangian Integrated Trajectory) model backwards run trajectories, clustered into 7 groups

(shown in Figure 3.1) using k-means clustering and the 'Openair' package in R. Hourly bioCO_2[APO] calculated in Equation 1 was used as the pollutant of interest and in the RF models as the obsevation variable. 80% of the input data was used to train the model and the other 20% was used to validate the model predictions.

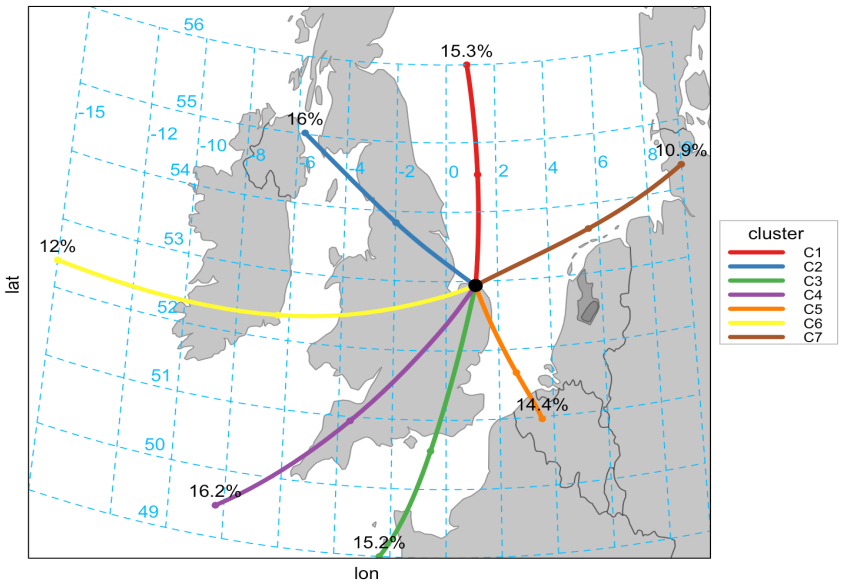

Figure 3.1. The seven back trajectory clusters for the WAO receptor location between 01/01/2011-31/07/2020 which were used by the RF bioCO_2 models. The clusters are decoded in Appendix B – Table B1 and the percentages indicate the frequency of occurrence.

The trained model was then used to predict the 'counterfactual bioCO_2' that would have been observed at WAO during the periods 01/08/2015-31/05/2016 and 01/08/2019-31/05/2020 if the warm winters had not occurred. These two counterfactual predictions were then compared to their respective observation-derived bioCO_2[APO] values to further estimate the impact of warm winter detected at WAO.

Partial dependency and variable importance graphs were also created using functions in the 'rmweather' package to achieve objective 3.

3.3. Uncertainty

Since the bioCO_2 values were calculated by subtracting ffCO_2[APO] from the measured CO_2, and the measure of CO_2 was essentially assumed to be correct (there is some uncertainty in the CO_2 measurement, which was already accounted for in the measurement uncertainty of APO part and in any case is negligible, < 1%), the sources of uncertainty in bioCO_2 were,

therefore, considered to be the same as in the continuous APO-based $ffCO_2$ quantification approach which are associated with each term in Equation 2. Calculations of $ffCO_2$[APO] uncertainties were explained in details in Pickers et al. (2020) and summed up in Table 3.1.

Table 3.1. Hourly uncertainty estimates for $ffCO_2$[APO] at WAO (Pickers et al., 2020).

	$ffCO_2$[APO] or $bioCO_2$[APO]
Background uncertainty (APO_{bg})	±28%
Measurement uncertainty (APO)	±04%
Time-varying ratio uncertainty (R_{APO})	±23%
Total uncertainty	±36%

Since a mean R_{APO} value was used in the $ffCO_2$[APO] calculation for this study instead of time-varying R_{APO} values, the uncertainty associated with this ratio is doubled from 23% to 46%. This increases the total uncertainty of $ffCO_2$[APO] or $bioCO_2$[APO] from 36% to 54% for the hourly value Pickers et al. (2020), which decreases to 10% for the daily value and 8% for the monthly value. The estimated 10% value for daily uncertainty was calculated by squaring the hourly uncertainties values at 54%, summing them all together over 24 hours, taking the square root of the total 24-hour uncertainty value, and calculating how large this was relative to the total $ffCO_2$ value over 24 hours. The monthly uncertainty was estimated similarly over the number of hours in each specific month.

In the ML analysis, the same $bioCO_2$[APO] uncertainties as stated in Table 3.1 were used. The uncertainty associated with the ML algorithm was also considered. Additional uncertainty of ±45% (±40%) was assigned to the 2015/16 (2019/20) 'counterfactual case' to account for this. This uncertainty was estimated by comparing the predicted 'counterfactual case' to the predicted 01/08/2018-31/04/2019 $bioCO_2$, which was generated from a separate model that was trained on the 01/01/2011-31/07/2018 data (excluding the 01/08/2015-31/05/2016 period as it includes the 2015/16 warm winter). Predictions for normal years from model running on previous years of data in this way do not have erroneous warm winter signals (which should occur if the model prediction was consistently prone to overestimation) (Pickers et al., 2020).

The differences between the $bioCO_2$ results of each period were compared to the 95% confidence interval (CI; 95% CI = standard deviation × 1.96) limits of the data; differences

between each period results were deemed significant if they exceeded the mean CIs of the time series data.

4. Results and discussion

4.1. Seasonal cycles

The bioCO_2[APO] seasonal cycle observed at WAO was affected by the warm winters during the 2015/16 (green line) and 2019/20 (blue line) periods (Figure 4.1). During these two periods, there was an increase in the seasonal amplitude compared to the mean (red line) (Figure B1 in the Appendix B and figure 4.1). While the overall patterns of both periods compared well with the mean, the high bioCO_2 concentrations normally observed between October and February were further increased between December and February. For the 2019/20 period, the monthly CO_2 anomalies (blue line minus red line) were 0.70 ± 0.23 ppm, 1.61 ± 0.52 ppm, and 1.74 ± 0.42 ppm in December, January and February respectively, which correspond to 16%, 32% and 40% increases from the mean bioCO_2. Similarly, in the 2015/16 series, the monthly CO_2 anomalies (green line minus red line) were 1.80 ± 0.21 ppm, 1.42 ± 0.55 ppm, and 1.21 ± 0.47 ppm corresponding to 39%, 35% and 28% increases from the mean bioCO_2 for those three winter months respectively. Even though these increases were not statistically significant (at 95% confident level (CL)), they could still be practically significant in that they could be associated with a stronger net CO_2 release during this period, possibly coupled with a strong warming-induced ecosystem respiration enhancement. Indeed, it is noticeable that during the three winter months, the bioCO_2 concentration of both periods shared the same patterns with their temperature trends (Figure 2.2 and 4.1). The 2019/20 three-month winter had higher temperatures and higher bioCO_2 around the beginning of December period while the 2015/16 trends peaked around February. Similar to Commane et al. (2017) and Liu et al. (2019) which focused on high-latitude responses, this mid-latitude study also found an increase in terrestrial CO_2 with increasing winter temperatures supporting the idea that warm winters could cause ecosystems to potentially become a net CO_2 source.

The net increase in bioCO_2 in the 2019/20 winter period was partially compensated by a greater increase in CO_2 uptake in the following April and May 2020. The observation comparison suggests that the monthly CO_2 anomalies in April and May 2020 were about -1.91 $\pm$ 0.12 ppm (-75% relative to the mean bioCO_2) and -1.52 $\pm$ 0.01 ppm (-53%) respectively (Figure 4.1). The statistically insignificant negative differences (at 95% CL) in these two months could possibly be promoted by extremely warm and sunny conditions with moderate rainfall deficits in April and May 2020. It is possible that the productivity gaining from increasing photosynthesis, and earlier budburst (Badeck et al., 2004; Salmon et al., 2016)

with increasing temperature and sunlight outweighed the carbon release from warming-induced enhancement in ecosystem respiration during those two months.

Unlike the 2019/20 period, there were no negative anomalies observed in spring 2016 but marginally higher bioCO_2 concentrations than the mean by 0.53 ± 0.84 ppm (+16%), 0.82 ± 0.41 ppm (+35%) and 0.35 ± 0.20 ppm (+14%) in March, April and May respectively. These positive anomalies were not statistically significant (at 95% CL) but again could still be practically significant. The 2015/16 spring period in England was characterized by a particularly cold and dry snap with limited sunlight in April and May, limiting plant growth, and therefore decreasing the carbon uptake, resulting in a higher concentration than the mean. Additionally, this period had a settled weather system with light wind patterns, which could decrease dispersions of CO_2-enriched air from any perturbation of biogenic CO_2 fluxes resulting in a weather-related atmospheric CO_2 enrichment (Higuchi et al., 2003).

These analyses suggest that temperature could play an important role in controlling winter-spring net carbon in the mid-latitude region. The "warmer spring, bigger spring carbon sink" mechanism could still be applied in my study. Similar to Wolf et al. (2016) and Liu et al. (2019) discussed in the literature review section, the results of this study further highlight the importance of the spring carbon sink as a natural mitigation for processes increasing CO_2 or lowering the terrestrial carbon uptake. Temperature-influenced increases in terrestrial CO_2 uptake in spring has been recognized as one of the main processes regulating the strength of terrestrial carbon uptake in the northern hemisphere in past decades (Ciais et al., 2019). However, the sensitivity of terrestrial CO_2 uptake to temperature during spring time has been shown to be weakening in recent decades (Piao et al., 2017).

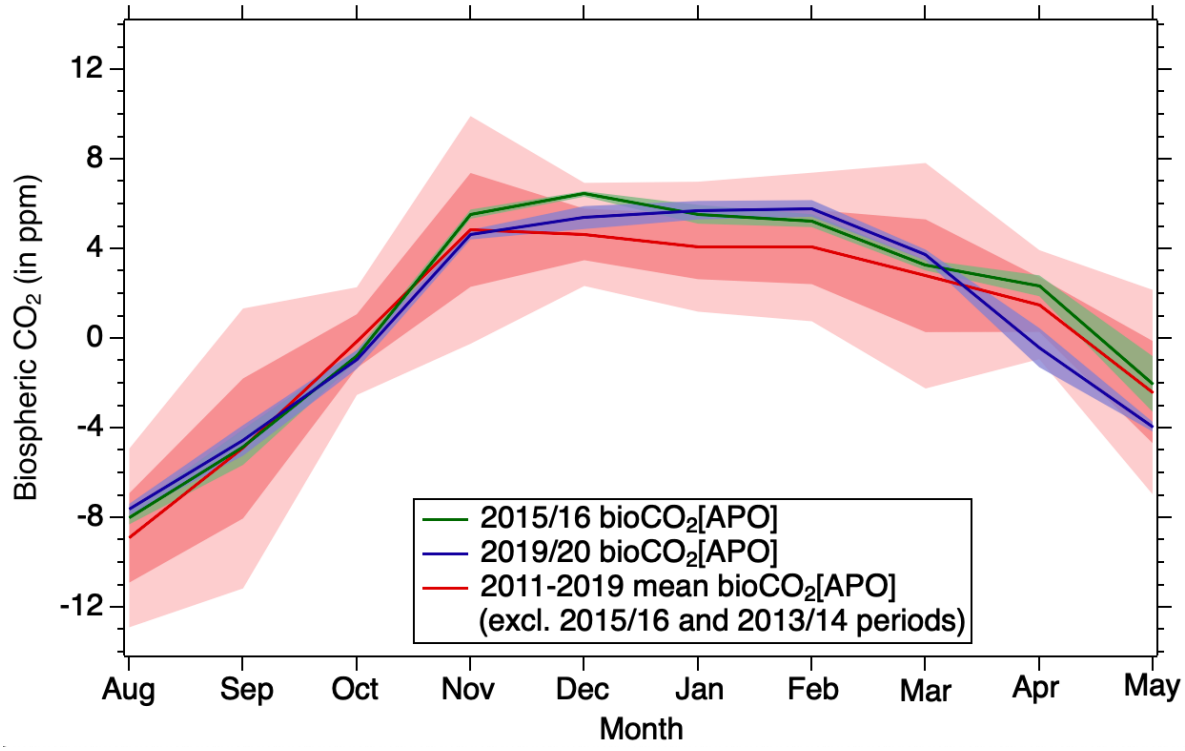

Figure 4.1. Monthly APO-derived $bioCO_2$ concentration (in ppm) at WAO for periods running from the beginning of August to the end of May. The 2015/16 period is shown in green, 2019/20 in blue and the baseline mean (01/08/2011-31/07/2019 excluding the 01/08/2015-31/07/2016 period as this period includes 2015/16 warm winters and the 01/08/2013-31/07/2014 period due to large gaps in APO data) in red. The green and blue shadings are monthly uncertainty estimates of $ffCO_2$[APO] at WAO for the 2015/16 and 2019/20 periods respectively; the dark red shading and the light red shading are respectively 1σ (68% CI) and 2σ (95% CI) away from the monthly mean value.

4.2. Diurnal cycles

Figure 4.2 displays the diurnal cycles of $bioCO_2$ for each month in the August-May period. The concentration of $bioCO_2$ experienced an overnight increase. The observations at WAO are taken from a height of 10 m above ground level, thus always within the well-mixed Planetary Boundary Layer (PBL). The diurnal rectifier effect, therefore, could have a role in the observed diurnal cycles (Stephens et al., 2000). During daytime in the growing season, there was a rapid decrease in CO_2 concentration due to photosynthetic processes and rapid development of the surface turbulent layer as the ground heats up (Higuchi et al., 2003). During night time, photosynthesis halts while soil and plant respiration begins, resulting in a net source of CO_2. This CO_2-enriched air builds up in a stable nocturnal boundary layer formed by a temperature

inversion as a result of surface radiative cooling, leading to a rapid increase in CO_2 concentration during the night (Higuchi et al., 2003). Shortly after sunrise, the stable layer collapses causing the accumulation to stop and the cycle repeats (Higuchi et al., 2003). This rectifier effect appears to be less intense during the winter season (December–February) (Figure 4.2) resulting in a lower amplitude of the diurnal cycles by around 7.00 ppm as seen in Figure 4.3 as the PBL remains lower for longer due to lower temperatures (Stephens et al., 2000), and terrestrial photosynthesis activity is also reduced due to decreased sunlight hours.

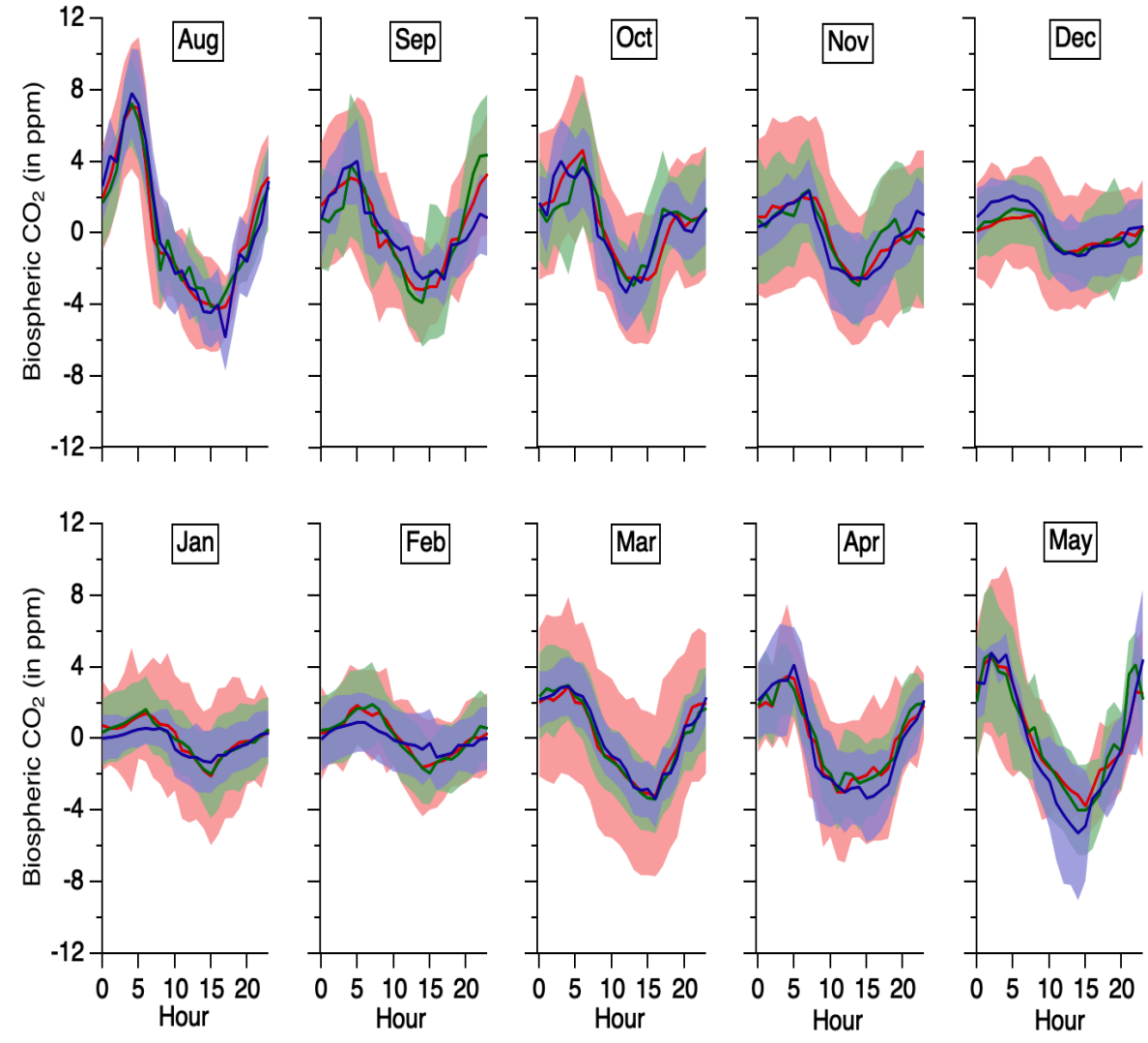

Figure 4.2. Diurnal cycles for each month in the August – May period. The green, blue and red lines are 2015/16, 2019/20 periods and the baseline mean respectively. The green, blue and red shadings are each period's respective uncertainty (2σ away from the hourly mean values).

The monthly amplitude of the daily cycle observed at WAO was noticeably 0.80 ppm smaller than the mean in January 2020, and even 1.91 ppm smaller in February (Figure 4.3). Following that were increases in the amplitude of 1.12 ppm and 1.54 ppm in April and May 2020 respectively. It turns out that the variability in the observed diurnal CO_2 amplitude could be primarily driven by the night-time CO_2 concentration (Schmidt et al., 2014), which is regulated mostly by the daily changes in PBL dynamics influenced by synoptic weather conditions as suggested by previous studies (Xueref-Remy et al., 2018, Fang et al., 2014; Garcia et al., 2012; Gerbig et al., 2006).

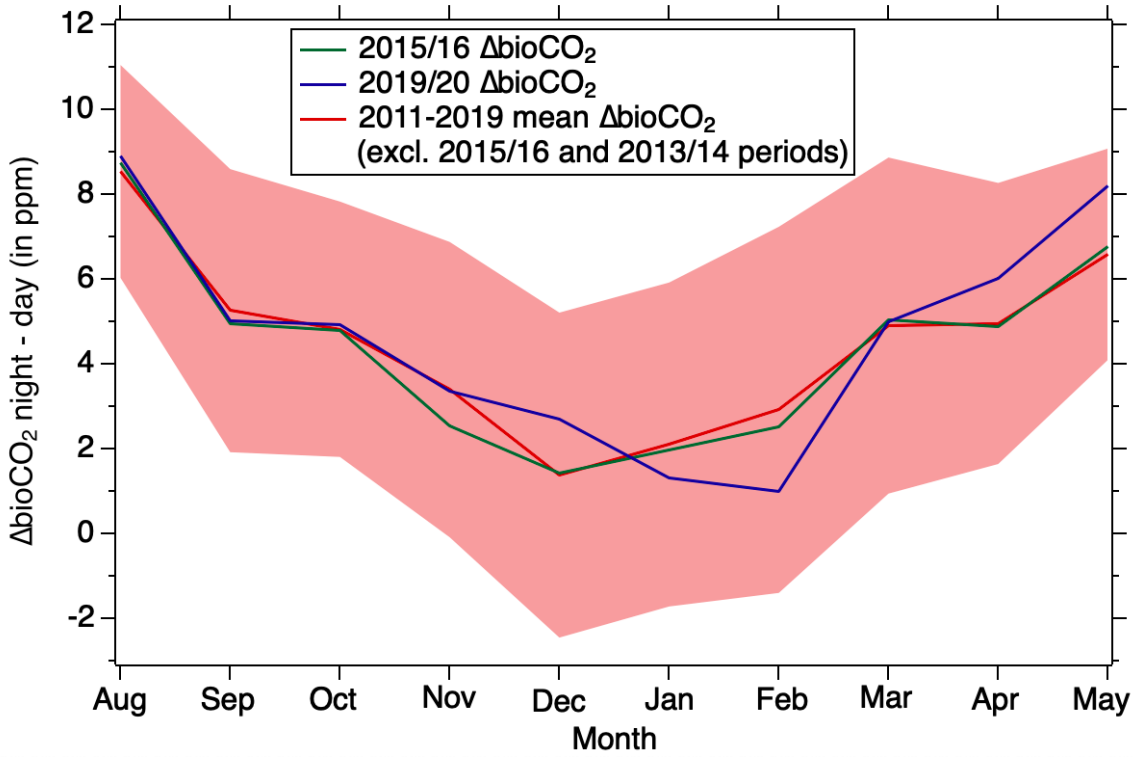

Figure 4.3. The monthly amplitude of the CO_2 daily cycles (in ppm) for periods running from the beginning of August to the end of May the next year. The green, blue and red lines are the 2015/16, 2019/20 periods and baseline mean respectively. The red shading is 2σ away from the hourly mean values or 95% CI.

The months of January and February 2020 were exceptionally stormy with mean daytime and night-time wind speeds of 9.80 m s^{-1} and 9.70 m s^{-1} respectively for January and 10.00 m s^{-1} and 11.00 m s^{-1} for February at WAO (Appendix B – Figure B2 and B3). Unsettled and windy conditions tend to destabilise atmospheric stratification allowing more

mixing, lowering night-time concentration, and therefore producing a smaller diurnal cycle of bioCO_2 (Fang et al., 2014). April and May 2020 were exceptionally warm, sunny and calm favouring photosynthesis, and resulting in an increase in the surface uptake by ecosystems and therefore a decrease of the daytime concentrations while increasing respiration and stabilizing stratification near the surface at night allowed high concentrations of CO_2 to accumulate. This resulted in the increases in the bioCO_2 daily amplitude in those two months.

4.3. Random forest prediction

a. Model evaluation

The predictive RF model performed well for WAO station. The bias and R^2 value for the model are displayed in Appendix B – Figure B4. The R^2 value is 0.74. This suggests that bioCO_2 concentrations at WAO predicted by an RF model with a combination of surface meteorological conditions, temporal factors and back trajectory air mass clusters are reliable.

The most important influencing variable for bioCO_2 concentrations is demonstrated in Figure 4.4. Day Julian and temperature were the most important variables influencing the variability in bioCO_2 concentrations. This suggests that temperature and the seasonal cycle have a significant impact on bioCO_2 concentrations. The least significant variables in the RF model were the day of the week and wind speed, but both variables were still added to the predictive performance of the model. Including variables with low predictive potential does not negatively affect the accuracy of the model, hence they were retained in the model. Wind direction was one of the most unimportant variables. This could be because its hourly aggregation interval might be too long to adequately represent the atmospheric motion. Wind direction, hence, did not add much information to the bioCO_2 predictions of the model.

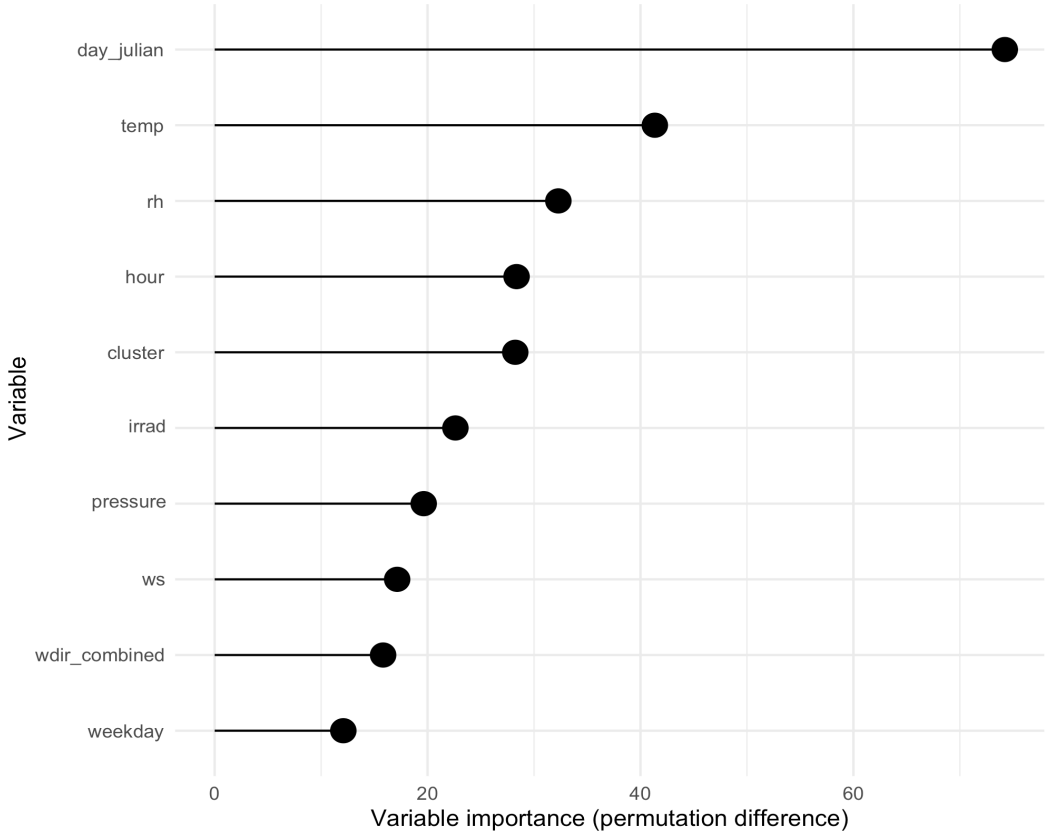

Figure 4.4. Variable importance plot for bioCO_2 for WAO.

b. ‘Counterfactual cases’ of 2015/16 and 2019/20 winters

Overall, the model predictions for three different periods were less variable than their APO-derived observations (Figure 4.5). The trend of the prediction for a normal period (2011/12 in this case) fitted quite well with that of the observation (Figure 4.5a). This again showed that the model performed well with the data obtained from WAO and did not suffer from overfitting. Sustained increases in the daily bioCO_2[APO] relative to the counterfactual predictions from December to February averaging 1.81 ± 0.23 ppm (+26% relative to the counterfactual prediction) and 2.10 ± 0.42 ppm (+30%) in the 2015/16 and 2019/20 periods respectively were found (Figure 4.5). These anomalies again confirm the potential effect of the warm winters on the bioCO_2 at WAO. The influence of warm winters on bioCO_2 detected at WAO was further highlighted in the cumulative signal, shown in Figure 4.6, which accumulates differences in the short-term variability of the daily values. Both warm winters have statistically significant sharp increases (at 95% CL) in the cumulative differences. The 2015/16 trend continued to increase slowly around April to May while the 2019/20 difference decreased around springtime. These are similar to what has been observed in the previous

seasonal observational interpretations (Figure 4.1). It is also interesting to notice the influences of the 2018 cold period from mid-February to the beginning of March associated with 'Beast from the East' event on bioCO_2 concentrations in figure 4.6 (the yellow line). There was a decrease in the cumulative differences indicating the bioCO_2[APO] was smaller than the predicted counterfactual case for that period, possible coupled with low temperatures reducing plant respiration and heavy snow cover hindering spring growth.

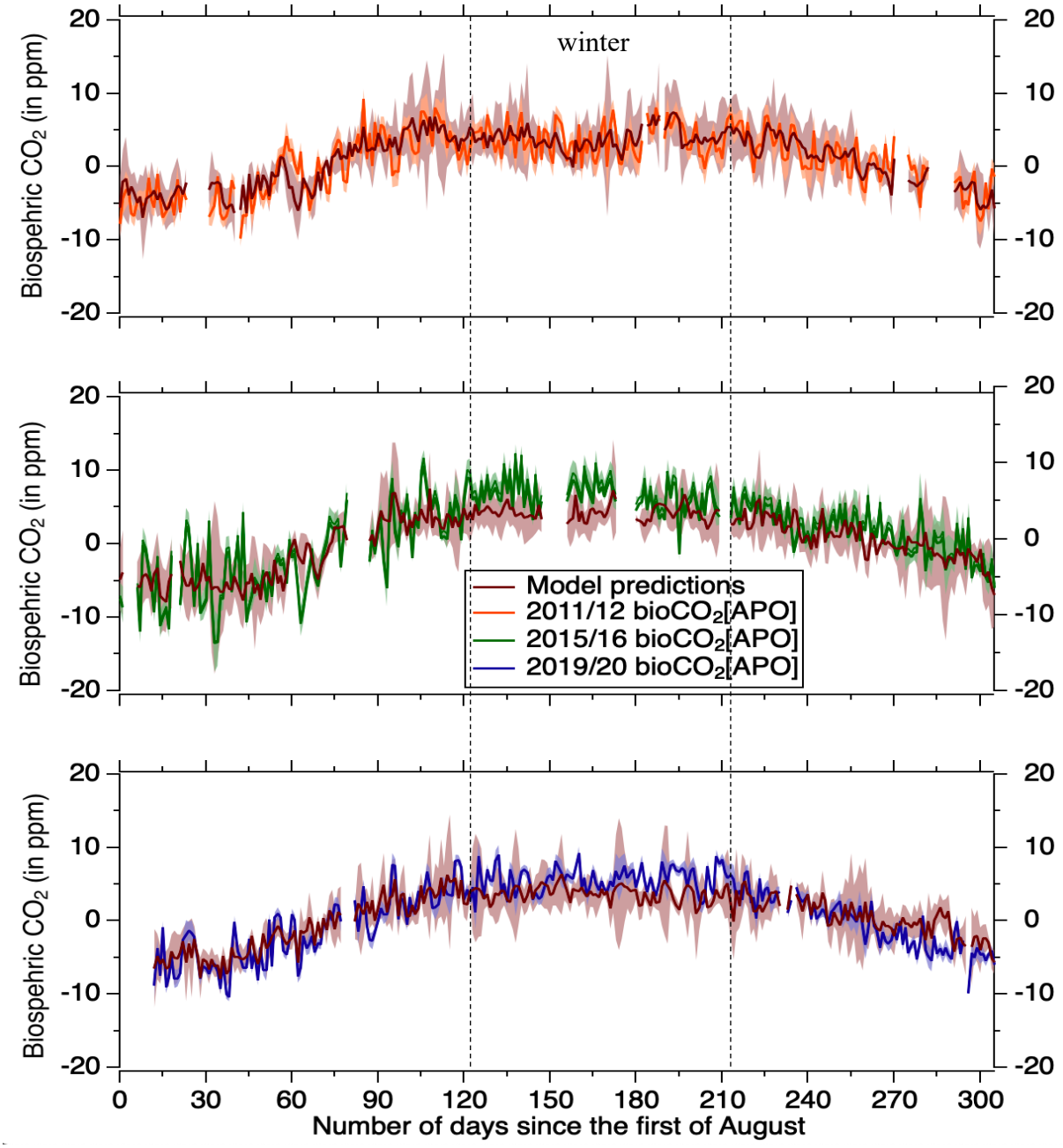

Figure 4.5. Daily $bioCO_2$ concentration (in ppm) of APO-derived observations and model predictions for the period from the beginning of August to the end of May the following year. Orange, green and blue lines are APO-derived concentrations for the 2011/12, 2015/16 and 2019/20 periods respectively; brown lines are model predictions for each specific period (the predicted period is omitted from the respective training model). Orange, green and blue shadings are hourly uncertainty estimates for $ffCO_2$[APO] for respective periods; brown shading indicates the total uncertainty in the analysis (i.e. the combined uncertainty from $ffCO_2$[APO] quantification and the ML).

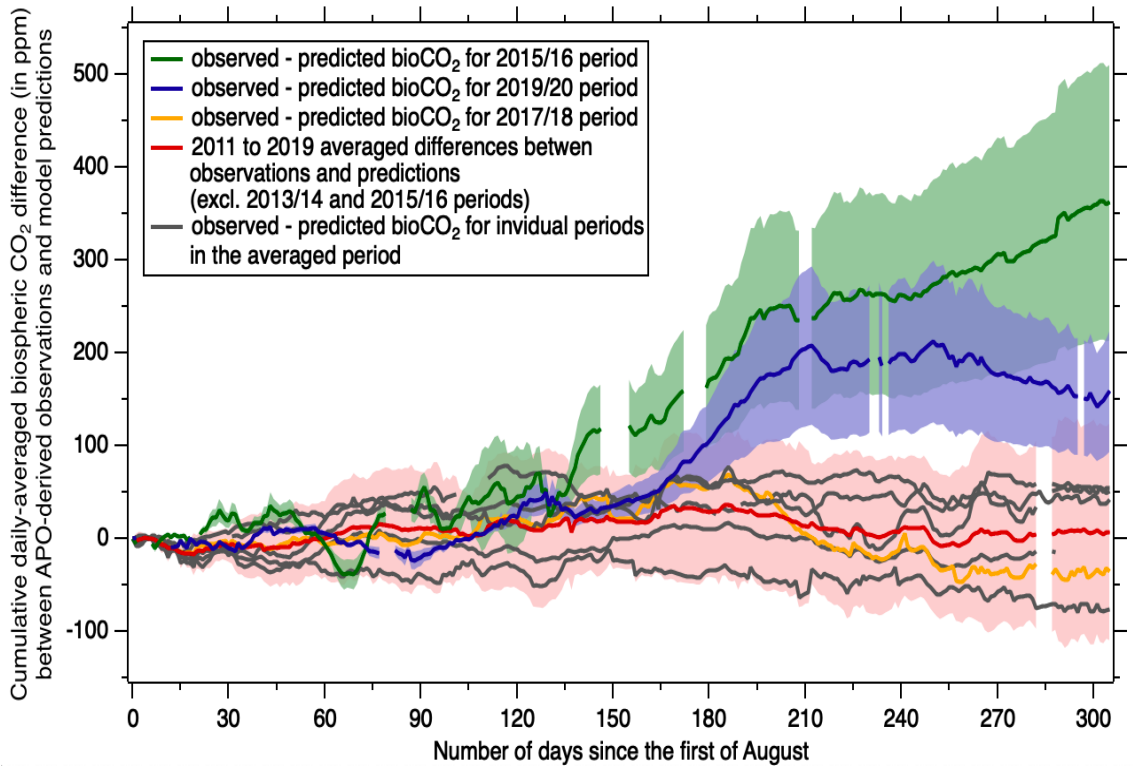

Figure 4.6. The green, blue and yellow lines are cumulative daily bioCO$_2$ differences (in ppm) (APO-derived observations minus modelled) for the 2015/16, 2019/20, and 2017/18 periods respectively. The black lines are the cumulative bioCO$_2$ differences for individual periods from the 01/08/2011-31/07/2019 (excluding the 01/08/2015-31/07/2016 period as this period includes 2015/16 warm winters and the 01/08/2013-31/07/2014 period due to large gaps in APO data) and the red line is the mean of all these individual periods. Uncertainties are as follows: the red shading is the ± 2σ (95% CI) standard deviation of the 2011-2019 mean; the green and blue shadings indicate the total uncertainty in the analysis (i.e. the combined uncertainty from bioCO$_2$[APO] quantification and ML) for the 2015/16 and 2019/20 periods respectively.

c. Explaining the relationships between bioCO$_2$ and meteorological variables in the counterfactual cases.

One of the advantages of RF that other ML techniques do not have is the ability to investigate and explain the models. Partial dependence plots are used to analyse RF models by explaining how influencing variables were used in generating prediction (Jones and Linder, 2015). The application of partial dependence plots, hence, could be used to explain some general physical and chemical processes. For example, in figure 4.7, bioCO$_2$ concentration is

lower during daytime and higher during night time mainly due to the rectifier effect as explained above, and wintertime concentrations are higher than other seasons resulting from a combination of a greater CO_2 source from ecosystem respiration and atmospheric stability during the winter.

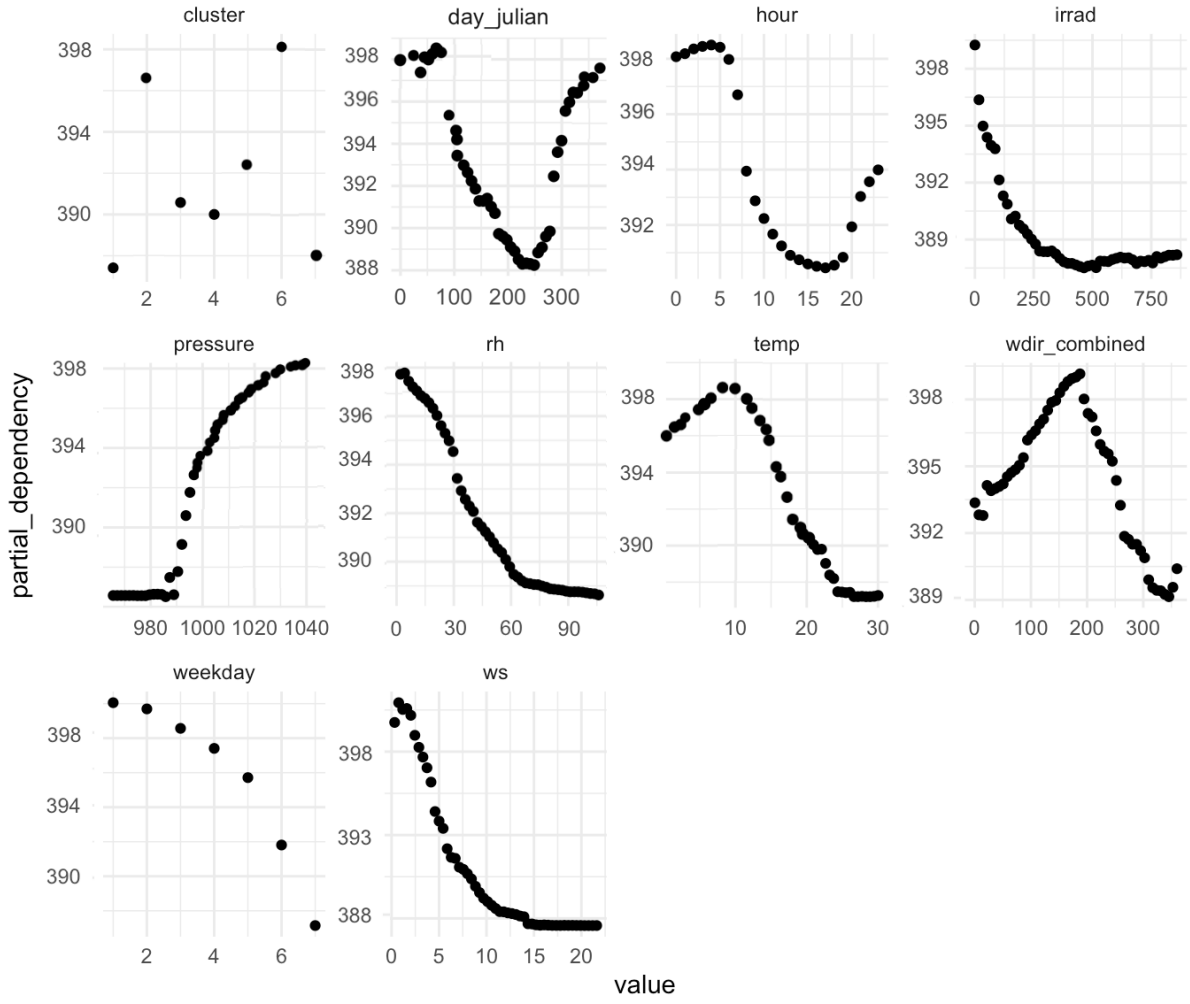

Figure 4.7. Partial dependence plots of the influencing variables used in bioCO_2 RF model at WAO. y (vertical) axes for each plot represent the bioCO_2 concentration and x (horizontal) axes show the corresponding influencing variables.

The pattern of irradiation component was similar to air temperature (Figure 4.7). The similar shapes of bioCO_2 variations with these variables describe rather the same process. Increasing temperature with increasing irradiation could have favoured photosynthetic processes and therefore increased the CO_2 uptake rate leading to lower bioCO_2 concentration. At temperatures between 10.00 and 20.00°C, photosynthetic enzymes work at their best

(Qaderi and Reid, 2008), resulting in high photosynthetic rates leading to a decrease of 12.00 ppm in the bioCO_2 concentration. At temperatures above 20.00°C, the concentration of bioCO_2 plateaus at 386 ppm because above 20.00°C photosynthetic enzymes lose their shape and functionality and therefore do not work efficiently anymore (Qaderi and Reid, 2008). It is also noticeable that below 10.00°C, the bioCO_2 concentration increases with increasing temperature. Temperatures below 10.00°C are representative of the winter period when respiration is the dominant temperature-dependent process that drives the variability of bioCO_2.

Relative humidity (RH) was the third important variable in predicting the bioCO_2 variations (Figure 4.4) and directly proportional to the bioCO_2 concentration (Figure 4.7). RH is a percentage measurement of the amount of moisture in the air relative to maximum saturation (how much moisture the air can hold when it is saturated) representing how much water vapour is in the air relative to how much that volume of air is capable of holding. The closer to 100% the RH is, the more humid the atmosphere. Therefore, decreasing RH results in increasing vapour pressure deficit (VPD) which is the difference (deficit) between the amount of water vapour in the air and maximum saturation. An increase in VPD could lead to stomatal closure in plants to reduce water loss. This stomatal closure could lead to a reduction in photosynthetic rates and therefore lower CO_2 uptake (Grossiord et al., 2020). Hence, the lower RH, the higher VPD, the lower CO_2 uptake, hence the more elevated the CO_2 concentration in the atmosphere as seen in figure 4.7.

The back trajectory cluster variable was important for WAO monitoring sites . The two air masses 2 and 6 representing local flows from Northern Ireland and a strong westerly flow from the Atlantic, respectively, have the highest concentration (Figure 4.7 and 3.1). This indicates that air masses originating from western UK crossing mainland England could create high concentration bioCO_2 conditions at WAO.

Pressure and wind speed were less important for the RF model but their partial dependence plots still demonstrate what would be expected. Although the pressure component showed an opposite pattern to windspeed (Figure 4.7), they both had somewhat the same processes. High surface pressure general leads to settled weather conditions with light winds resulting in decreased atmospheric dispersion and therefore lower bioCO_2 concentration and vice versa with low surface pressure.

5. Conclusions

5.1. Summary of key findings

A better understanding of the seasonal response of the terrestrial biosphere to weather extremes associated with climate change provides important insights for future carbon-climate feedbacks and their consequences on atmospheric CO_2 dynamics in the northern hemisphere. This study has investigated the influences of 2015/16 and 2019/20 warm-winter-to-spring transition periods on the bioCO_2 concentrations derived from observational APO. The specific conclusions relating to the three objectives of this study are as follows:

a. My study found that the increase in the seasonal maxima of bioCO_2 in 2015/16 and 2019/20 winters (DJF) is significant (at 95% CL) compared to their respective counterfactual cases (2015/16 and 2019/20 hypothetical winters without the warming) (Figure 4.6) but not significantly different (at 95% CL) from the 2011-19 mean (Figure 4.1). This result, however, could still be considered practically significant, indicating that warm winters could potentially make mid-latitude ecosystems a net source of CO_2. The apparent increase in CO_2 release in the 2019/20 warm winter appears to be partially offset by an apparent higher CO_2 uptake in the following warm spring (Figure 4.1). This results in a larger seasonal amplitude compared to the mean and nearly neutral effects on the annual net CO_2. In contrast, the 2015/16 spring period at WAO experienced a slightly weaker net CO_2 uptake than the mean (Figure 4.1), suggesting a delay in the growing season, with either continued CO_2 release by respiration from the warm winter months or a reduction in photosynthetic uptake driven by a cold snap and limited sunlight in the subsequent 2016 spring.
b. The minimum of the diurnal cycle occurs in the afternoon (14:00 to 17:00 UTC) when the PBL is well mixed, and during seasons when vegetation photosynthesis is active (Figure 4.2 and 4.3). It appeared that it was not the increase in temperature during the warm winter but the synoptic-related PBL dynamics that mainly influenced the amplitude of the bioCO_2 diurnal cycle. The amplitude of the diurnal cycle of bioCO_2 at WAO in 2019/20 was smaller and larger than the mean coupled with windy and calm weather conditions respectively.
c. The RF performed well with an R^2 value of 0.74. Temperature, Julian day (the seasonal component), and RH cluster were generally the most important predictors for bioCO_2 concentration (Figure 4.4). To explain the model predicted trends, partial dependence plots were used (Figure 4.7). The plots indicated that elevated bioCO_2 concentrations

occur in poor dispersion conditions (low windspeed) as well as at low temperatures and high RH.

5.2. Limitations and recommendations for further research

Apart from temperature, soil moisture is another important environmental parameter controlling terrestrial carbon exchange, especially in the late growing season because water stress could affect plant physiology and therefore their primary productivity and respiration rate (Liu et al., 2019). However, that variable has not been included in this study due to a lack of available data. Future continuations of this project should further investigate the influences of temperature, soil moisture and hydrology of warm winters on the bioCO_2 signals in the mid-latitudes.

This study has also presented a novel approach for deriving bioCO_2 from a top-down fossil fuel CO_2 quantification method using APO data. One of the assumptions in this study is that the bioCO_2 signals derived with this method are all terrestrial signals. However, bioCO_2 could also be significantly influenced by the ocean. Quantifying contributions of different components of the bioCO_2 signal (photosynthesis, respiration, oceanic influences) remains a difficult challenge and requires other types of data such as satellite observations which can complement surface measurements to better characterize spatial variability.

Another limitation with using observation-based APO to derived bioCO_2 is that it relies on very high-precision atmospheric O_2 measurements which are technically very challenging (Pickers, 2016). This has severely restricted APO's widespread implementation and the existing network of atmospheric O_2 measurements is sparse, with almost no measurement sites being ideally located to capture emissions from urban regions (Pickers, 2020). This results in the spatial limitations of this study which is confined to just one study location. To increase the spatial scale covering most warm-winter affected locations for further study on this topic, other observation-based methods, such as CO which is a more commonly measured trace gas, could be used, to quantify bioCO_2 as in Oney et al. (2017).

6. References

Atkin, O. K., Macherel, D. (2009) The crucial role of plant mitochondria in orchestrating drought tolerance, Annals of Botany, 103, 581–597.

Ballantyne, A. P., Andres, R., Houghton, R., Stocker, B. D., Wanninkhof, R. et al. (2015) Audit of the global carbon budget: Estimate errors and their impact. Biogeosciences 12(8), 2565–2584, ISSN 1726–4189.

Biau, G., Devroye, L., and Lugosi, G. (2008) Consistency of Random Forests and Other Averaging Classifiers, Journal of Machine Learning Research, 9, 2015–2033.

Bréda, N., Huc, R., Granier, A., Dreyer, E. (2006) Temperate forest trees and stands under severe drought: a review of ecophysiological responses, adaptation processes and long-term consequences. Annals of Forest Science, 63, 625 – 644.

Breiman, L. (2001) Random Forests, Machine Learning, 45, 5–32.

Buras, A., Rammig, A., and Zang, C. S. (2020) Quantifying impacts of the 2018 drought on European ecosystems in comparison to 2003, Biogeosciences, 17(6), 1655–1672.

Caruana, R. and Niculescu-Mizil, A. (2006) An empirical comparison of supervised learning algorithms, in: Proceedings of the 23rd international conference on Machine learning, Association for Computing Machine learning, 161–168.

Ciais, P., Reichstein, M., Viovy, N., Granier, A., Ogée, J., Allard, V., et al. (2005) Europe-wide reduction in primary productivity caused by the heat and drought in 2003, Nature, 437(7058), 529-33.

Ciais, P., Sabine, C., Bala, G., Bopp, L., Brovkin, V., Canadell, J., et al. (2013) Carbon and Other Biogeochemical Cycles. In: Climate Change 2013: The Physical Science Basis. Contribution of Working Group I to the Fifth Assessment Report of the Intergovernmental Panel on Climate Change [Stocker, T.F., Qin, D., Plattner, G.-K., Tignor, M., Allen, S.K., Boschung, J., et al. (eds.)]. Cambridge University Press, Cambridge, United Kingdom and New York, NY, USA.

Ciais, P., Tan, J., Wang, X., Roedenbeck, C., Chevallier, F., Piao, S.-L., ... Tans, P. (2019). Five decades of northern land carbon uptake revealed by the interhemispheric CO_2 gradient. Nature, 568(7751), 221–225.

Commane, R., Lindaas, J., Benmergui, J., Luus, K. A., Chang, R.-W., Daube, B. C., et al. (2017) Carbon dioxide sources from Alaska driven by increasing early winter respiration from Arctic tundra. Proceedings of the National Academy of Sciences of the United States of America, 114(21), 5361–5366.

Fang, S. X., Zhou, L. X., Tans, P. P., Ciais, P., Steinbacher, M., Xu, L., and Luan, T. (2014) In situ measurement of atmospheric CO_2 at the four WMO/GAW stations in China, Atmospheric Chemistry and Physics, 14(5), 2541–2554.

Fereday, D. R., Knight, J. R., Scaife, A. A., Folland, C. K., and Philipp, A. (2008). Cluster Analysis of North Atlantic–European Circulation Types and Links with Tropical Pacific Sea Surface Temperatures, Journal of Climate, 21(15), 3687-3703.

Fisher, E. M., and Knutti, R. (2014) Detection of spatially aggregated changes in temperature and precipitation extremes, Geophysical Research Letters, 41, 547–554.

Frank, D., Reichstein, M., Bahn, M., Thonicke, K., Frank, D., Mahecha, M. D., et al. (2015) Effects of climate extremes on the terrestrial carbon cycle: concepts, processes and potential future impacts. Global Change Biology, 21(8), 2861-2880.

Friedman, J., Hastie, T., and Tibshirani, R. (2001) The Elements of Statistical Learning, Data Mining, Inference, and Prediction, Vol. 1, 2nd Edn., Springer series in statistics, Springer : Berlin.

Garcia, M. A., Sanchez, M. L., and Perez, I. (2012) Differences between carbon dioxide levels over suburban and rural sites in Northern Spain, Environmental Science and Pollution Research, 19, 432–439.

Gerbig, C., Lin, J. C., Munger, J. W., and Wofsy, S. C. (2006) What can tracer observations in the continental boundary layer tell us about surface-atmosphere fluxes?, Atmospheric Chemistry and Physics, 6(2), 539–554.

Goeckede, M., Michalak, A. M., Vickers, D., Turner, D. P. and Law, B. E. (2010) Atmospheric inverse modelling to constrain regional-scale CO_2 budgets at high spatial and temporal resolution. Journal of Geophysical Research. 115(D15), 1–23. ISSN 0148-0227.

Granier, A., Reichstein, M., Bréda, N., Janssens, I., Falge, E., Ciais, P., et al. (2007) Evidence for soil water control on carbon and water dynamics in European forests during the extremely dry year: 2003, Agricultural and Forest Meteorology, 143(1-2),123-145.

Grossiord, C., Buckley, T.N., Cernusak, L.A., Novick, K.A., Poulter, B., Siegwolf, R.T.W., et al. (2020), Plant responses to rising vapor pressure deficit, New Phytologist Foundation, 226(6), 1550-1566.

Gurney, K. R., Baker, D., Rayner, P. and Denning, S. (2008) Interannual variations in continental-scale net carbon exchange and sensitivity to observing networks estimated from atmospheric CO_2 inversions for the period 1980 to 2005, Global Biogeochemical Cycles 22(GB3025), 1–17.

Gurney, K. R., Law, R.M., Denning, A.S., Rayner, P. J., Bousquet, P. B., Bruhwiler, Y. H., et al. (2004) Transcom 3 inversion intercomparison: Model mean results for the estimation of seasonal carbon sources and sinks, Global Biogeochemical Cycles, 18(GB1010), 1–18.

Higuchi, K., D. Worthy, D. Chan, and A. Shashkov (2003) Regional source/sink impact on the diurnal, seasonal and inter-annual variations in atmospheric CO_2 at a boreal forest site in Canada, Tellus, 55B, 115–125.

Huang, J., Zhang, X., Zhang, Q., Lin, Y., Hao, M., Luo, Y., et al. (2017) Recently amplified arctic warming has contributed to a continual global warming trend. Nature Climate Change, 7(12), 875–879.

Immitzer, M., Atzberger, C., and Koukal, T. (2012) Tree Species Classification with Random Forest Using Very High Spatial Resolution 8-Band WorldView-2 Satellite Data, Remote Sensor, 4, 2661.

IPCC (2013) Climate change 2013: the physical science basis. Contribution of Working Group I to the Fifth Assessment Report of the Intergovernmental Panel on Climate Change. Stocker et al. (eds.). Cambridge University Press, Cambridge, United Kingdom and New York, USA.

IPCC (2014) Summary for Policymakers. In: Climate Change 2014: Mitigation of Climate Change. Contribution of Working Group III to the Fifth Assessment Report of the Intergovernmental Panel on Climate Change [Edenhofer, O., Pichs-Madruga, R., Sokona, Y., Farahani, E., Kadner, S., Seyboth, K., et al. (eds.)]. Cambridge University Press, Cambridge, United Kingdom and New York, NY, USA.

IPCC (2018). Global Warming of 1.5°C. An IPCC Special Report on the Impacts of Global Warming of 1.5°C Above Pre-Industrial Levels and Related Global Greenhouse Gas Emission Pathways, in the Context of Strengthening the Global Response to the Threat of Climate Change, Sustainable Development, and Efforts to Eradicate Poverty, eds Masson-Delmotte, V., Zhai, P., Pörtner, H. O., Roberts, D., Skea, J., Shukla, P. R., et al. (Geneva: IPCC).

Jones, Z. and Linder, F. (2015) Exploratory Data Analysis using Random Forests, 73rd annual MPSA conference, Chicago : USA.

Keenan, T., Sabate, S., Gracia, C. (2010) The importance of mesophyll conductance in regulating forest ecosystem productivity during drought periods, Global Change Biology, 16, 1019–1034.

Kendon, M., McCarthy, M., Jevrejeva, S., Matthews, A., Sparks, T. and Garforth, J. (2020), State of the UK Climate 2019, International Journal of Climatology, 40(S1), 1-69.

Kotsiantis, S. B. (2013) Decision trees: a recent overview, Artificial Intelligence Review, 39, 261–283.

Koven, C. D., Ringeval, B., Friedlingstein, P., Ciais, P., Cadule, P., Khvorostyanov, D., et al. (2011) Permafrost carbon-climate feedbacks accelerate global warming. Proceedings of the National Academy of Sciences of the United States of America, 108(36), 14769–14774.

Larcher W (2003) Physiological Plant Ecology, Springer, Berlin.

Lawlor, D. W. (1995) The effects of water deficit on photosynthesis. In: Environment and Plant Metabolism – Flexibilty and Acclimation , 129 – 160. Bios Scientific Publishers, Oxford.

Le Quéré, C., Andrew, R. M., Canadell, J. G., Sitch, S., Korsbakken, J. I., Peters, G. P., et al. (2016) Global carbon budget, Earth System Science Data, 8(2).

Liu, Z., Kimball, J. S., Parazoo, N. C., Ballantyne, P. A., Wang, J. W., Madani, N., et al. (2020) Increased high-latitude photosynthetic carbon gain offset by respiration carbon loss during an anomalous warm winter to spring transition, Global Change Biology, 26(2), 682–696.

Lobell, D. B,, Sibley, A., Ortiz-Monasterio, J. I. (2012) Extreme heat effects on wheat senescence in India, Nature Climate Change, 2, 1–4.

Lollar, B., 2014. Treatise on geochemistry. 1st ed. Amsterdam: Elsevier.

Lueker, T. J., Walker, S. J., Vollmer, M. K., Keeling, R. F., Nevison, C. D., Weiss, R. F., and Garcia, H. E. (2003) Coastal upwelling air-sea fluxes revealed in atmospheric observations of O_2/N_2, CO_2 and N_2O, Geophysical Research Letter., 30(25), 1–4.

McCarthy, M., Spillane, S., Walsh, S. and Kendon, M. (2016) The meteorology of the exceptional winter of 2015/2016 across the UK and Ireland, Weather, 71(12), 305-313.

Mueller, B., Seneviratne, S. I. (2012) Hot days induced by precipitation deficits at the global scale. Proceedings of the National Academy of Sciences of the United States of America, 109, 12398–12403.

Natali,S.M.,Schuur,E.A.G.,Trucco,C.,Pries,C.E.H.,Crummer,K.G.,&Lopez, A. F. B. (2011) Effects of experimental warming of air, soil and permafrost on carbon balance in Alaskan tundra. Global Change Biology, 17(3), 1394–1407.

National Climate Information Centre (2016), UK seasonal weather summary Spring 2016, Weather, 71(7), 169-169.

Niu, S., Luo, Y., Li, D., Cao, S., Xia, J., Li, J., et al. (2014) Plant growth and mortality under climatic extremes: an overview, Environment and Experimental Botany, 98, 13–19.

Noormets, A., McNulty, S. G., DeForest, J. L., Sun, G., Li, Q., Chen, J. (2008) Drought during canopy development has lasting effect on annual carbon balance in a deciduous temperate forest. New Phytologist, 179(3), 818-28.

Oney, B., Gruber, N., Henne, S., Leuenberger, M. and Brunner, D., (2017) A CO-based method to determine the regional biospheric signal in atmospheric CO_2. Tellus B: Chemical and Physical Meteorology, 69(1), 1353388.

Oney, B., Henne, S., Gruber, N., Leuenberger, M., Bamberger, I., Eugster, W., et al. (2015) The CarboCount CH sites: Characterization of a dense greenhouse gas observation network, Atmospheric Chemistry and Physics, 15(19), 11147–11164.

Palacio, S., Hoch, G., Sala, A., Körner, C., Millard, P. (2014) Does carbon storage limit tree growth?, New Phytologist, 201, 1096–1100.

Peylin, P., Law, R. M., Gurney, K. R., Chevallier, F., Jacobson, A. R., Maki, T., et al. (2013) Global atmospheric carbon budget: Results from an ensemble of atmospheric CO_2 inversions, Biogeosciences, 10(10), 6699–6720.

Piao, S., Liu, Z., Wang, T., Peng, S., Ciais, P., Huang, M., ... Tans, P. P. (2017). Weakening temperature control on the interannual variations of spring carbon uptake across northern lands. Nature Climate Change, 7(5), 359–367.

Pickers, P. A., (2016) New Applications of Continuous Atmospheric O_2 Measurements: Meridional Transects Across the Atlantic Ocean, and Improved Quantification of Fossil-Fuel derived CO_2. Ph.D. School of Environmental Science, University of East Anglia, Norwich, UK.

Pickers, P. A., Manning C. A., Le Quéré, C., Gerbig, C., Hoshina, Y., Tohjima, Y., et al. (2020) Quantifying fossil fuel CO_2 using atmospheric O_2 observations. In submission.

Qaderi, M., and Reid, D. (2008). Combined Effects of Temperature and Carbon Dioxide on Plant Growth and Subsequent Seed Germinability of Silene noctiflora, International Journal of Plant Sciences, 169(9), 1200-1209.

Ramonet, M., Ciais, P., Apadula, F., Bartyzel, J., Bastos, A., Bergamaschi, P., et al. (2020) The fingerprint of the summer 2018 drought in Europe on ground-based atmospheric CO_2 measurements, Philosophy Transactions of the Royal Society, 375(1810).

Regnier, P., Friedlingstein, P., Ciais, P., Mackenzie, F. T. and Gruber, N. (2013) Anthropogenic perturbation of the carbon fluxes from land to ocean. Nat. Geosci. 6(8), 597–607. ISSN 1752-0894.

Reichstein, M., Ciais, P., Papale, D., Valentini, R., Running, S., Viovy, N., et al. (2007) Reduction of ecosystem productivity and respiration during the European summer 2003 climate anomaly: a joint flux tower, remote sensing and modelling analysis, Global Change Biology, 13, 634-651.

Reichstein, M., Bahn, M., Ciais, P., Frank, D., Mahecha, M. D., Seneviratne, S. I., Zscheischler, J., et al. (2013) Climate extremes and the carbon cycle, Nature, 500(7462), 287–295.

Sarmiento, J. L., Gloor, M., Gruber, N., Beaulieu, C., Jacobson, A. R., Mikaloff Fletcher, S.E., et al. (2010) Trends and regional distributions of land and ocean carbon sinks. Biogeosciences, 7(8), pp.2351-2367.

Scaife, A. A., Comer, R., Dunstone, N., Fereday, D., Folland, C., Good, E., et al. (2017) Predictability of European winter 2015/2016. Atmospheric Science Letter, 18(2), 38-44.

Schaefer, K., Lantuit, H., Romanovsky, V. E., Schuur, E. A. G., & Witt, R. (2014) The impact of the permafrost carbon feedback on global climate. Environmental Research Letters, 9(8), 085003.

Schmidt, M., Lopez, M., Yver Kwok, C., Messager, C., Ramonet, M., Wastine, B., et al. (2014) High-precision quasi-continuous atmospheric greenhouse gas measurements at Trainou tower (Orléans forest, France), Atmospheric Measurement Techniques, 7, 2283–2296.

Severinghaus, J. P. (1995), Studies of the terrestrial O_2 and carbon cycles in sand dune gases and in Biosphere 2, Ph.D. thesis., Columbia University, New York.

Stephens, B.B., Wofsy, S.C., Keeling, R.F., Tans, P.P. and Potosnak, M.J., (2000) The CO_2 Budget and Rectification Airborne Study: Strategies for Measuring Rectifiers and Regional Fluxes. Geophysical Monograph-American Geophysical Union, 114, 311- 324.

Stephens, B.B., Wofsy, S.C., Keeling, R.F., Tans, P.P. and Potosnak, M.J., (2000) The CO_2 Budget and Rectification Airborne Study: Strategies for Measuring Rectifiers and Regional Fluxes. Geophysical Monograph-American Geophysical Union, 114, pp.311-324.

Tandon, A. and Schultz, A. (2020) Met Office: The UK's wet and warm winter of 2019-20. Available at: https://www.carbonbrief.org/met-office-the-uks-wet-and-warm-winter-of-2019-20 (Accessed date:13 Jun 2020).

Thompson, R. L., Broquet, G., Gerbig, C., Koch, T., Lang, M., Monteil, G., et al. (2020) Changes in net ecosystem exchange over Europe during the 2018 drought based on atmospheric observations, Philosophical Transactions of the Royal Society B: Biological Sciences, 375(1810).

Tong, W., Hong, H., Fang, H., Xie, Q., and Perkins, R. (2003) Decision Forest: Combining the Predictions of Multiple Independent Decision Tree Models, Journal of Chemistry Information and Computer Science, 43(2), 525–531.

Webb, E. E., Schuur, E. A. G., Natali, S. M., Oken, K. L., Bracho, R., Krapek, J. P., et al. (2016) Increased wintertime CO_2 loss as a result of sustained tundra warming. Journal of Geophysical Research: Biogeosciences, 121(2), 249–265.

Wolf, S., Keenan, T., Fisher, J., Baldocchi, D., Desai, A., Richardson, A., et al. (2016) Warm spring reduced carbon cycle impact of the 2012 US summer drought, Proceedings of the National Academy of Sciences, 113 (21), 5880-5885.

Xueref-Remmy, I., Dieudonne, E., Vuillenmin, C., Lopez, M., Lac, C., Schmidt, M. et al. (2018) Diurnal, synopic and seasonal variability of atmospheric CO_2 in the Paris megacity area, Atmospheric Chemistry and Physics, 18(5), 3335–3362 .

Zona, D., Gioli, B., Commane, R., Lindaas, J., Wofsy, S. C., Miller, C. E., et al. (2016) Cold season emissions dominate the Arctic tundra methane budget. Proceedings of the National Academy of Sciences of the United States of America, 113(1), 40–45.

7. Appendices

7.1. Appendix A: Results from additional journal papers

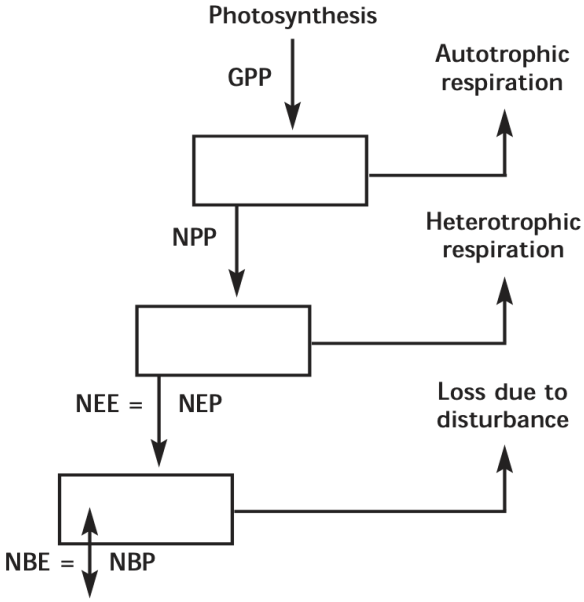

Figure A1. Diagrammatic representation of the main terms describing system carbon balances.

Gross primary production (GPP) refers to the total amount of carbon fixed in the process of photosynthesis by plants in an ecosystem. Net primary production (NPP) refers to the net production of organic carbon by plants in an ecosystem usually measured over a period of a year or more. It is GPP minus the amount of carbon respired by plants themselves in autotrophic respiration, R_a: $NPP = GPP - R_a$.

Net Ecosystem Exchange (NEE) and Net Ecosystem Production (NEP) refer to net primary production minus carbon losses in heterotrophic respiration, R_h: $NEP = -NEE = NPP - R_h$. NEE used more often to refer to these fluxes when they are addressed from a measurement of gas exchange rates using atmospheric measurements over time scales of hours, whereas NEP is more often used to refer to the same processes if measurements are based on ecosystem-carbon stock changes, typically measured over a minimal period of one year.

Net Biome Exchange (NBE) or Net Biome Production (NBP) refers to the change in carbon stocks after episodic carbon losses due to natural or anthropogenic disturbances have been taken into account:

$NBE = NEE - L_d$ or

$NBP = NEP - L_d$

where L_d is the loss by major episodic disturbances. Some systems are not typically affected by irregular disturbances.

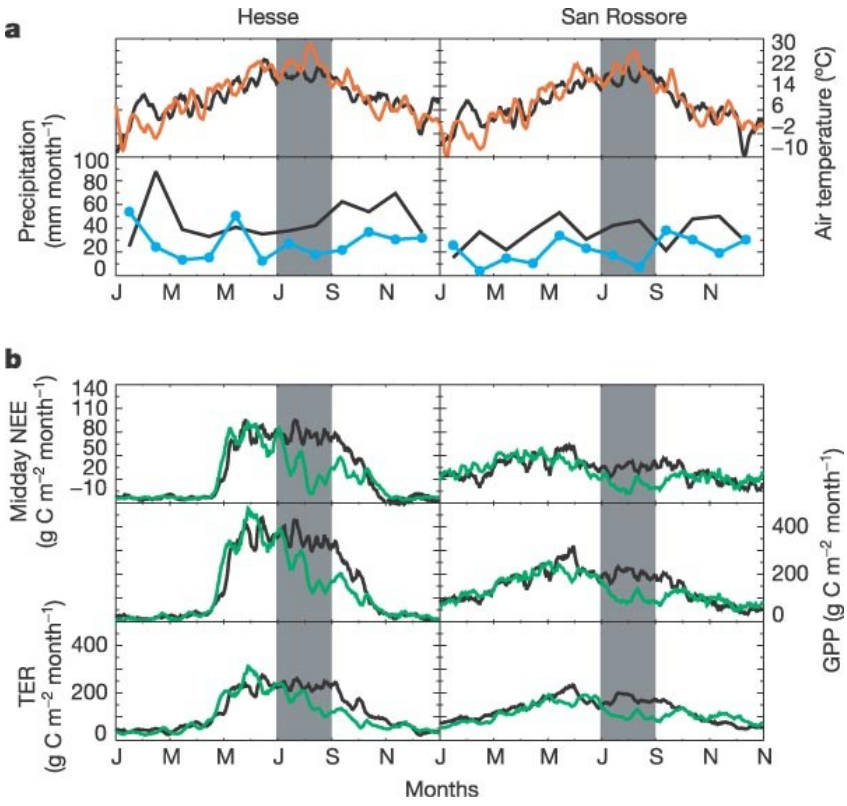

Figure A2. The two sites are a temperate deciduous beech forest in France (Hesse) and a southern evergreen pine forest site (San Rossore) in northern Italy. **a**, Climate fields. **b**, Ecosystem CO_2 fluxes from inversed model (Cias et al., 2005).

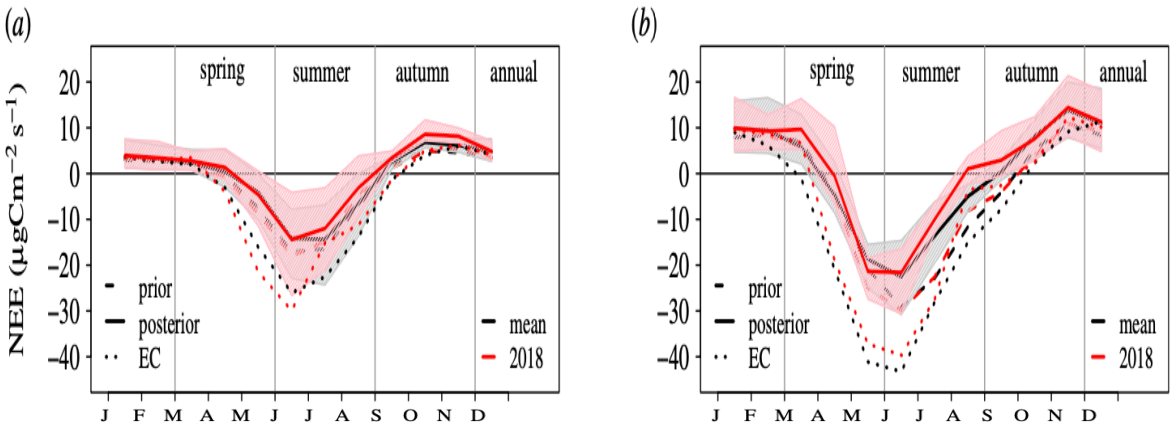

Figure A3. (a) Monthly mean NEE for the North region. For NEE, the mean of all months 2009–2018 is shown in black and the mean for 2018 is shown in red. The NEE anomaly is for 2018 compared to the mean 2009-2018 and is shown for the three inversion models by the solid lines and the range of all inversions in each case is shown by the shading. (b) Similar to (a) but for the Temperate region (Thompson et al., 2020).

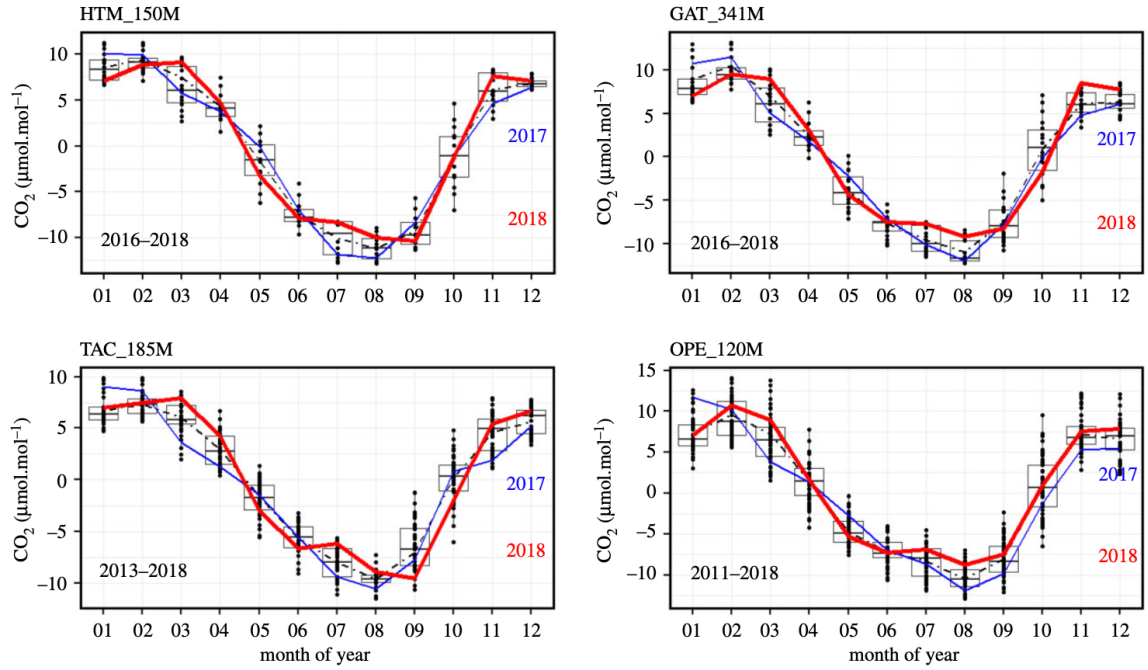

Figure A4. CO_2 seasonal cycles observed at Hyltemossa (HTM, Sweden), Gartow (GAT, Germany), Tacolneston (TAC, UK) and Observatoire Pérenne de l'Environnement (OPE, France). The 2018 cycle is shown in red, 2017 in blue, and a statistical summary of the full measurement period as box-and-whisker plots showing the median, first and third quartiles over the entire measurement period of each station, indicated in the bottom left corners of the plots (Ramonet et al., 2020).

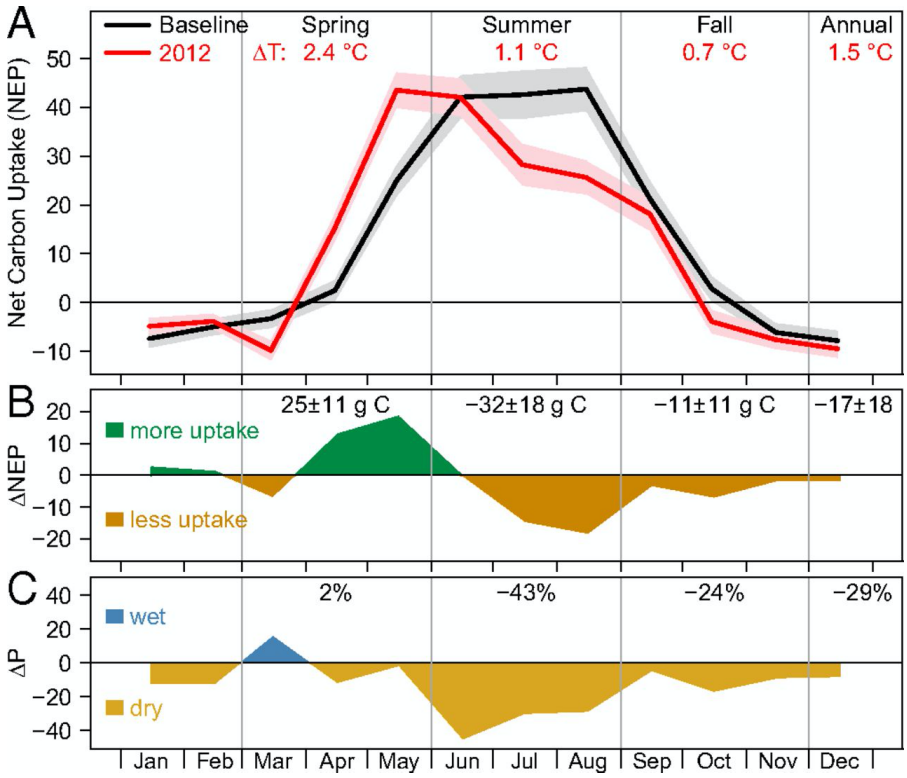

Figure A5. Net carbon uptake of concurrent warm spring and summer drought in 2012. (A) Ensemble mean of inversed modelled monthly NEP (g C m^{-2} mo^{-1}) for 2012 (red) and baseline (black) at sites that experienced drought during summer 2012 (n = 13). Numbers atop show the mean seasonal temperature (T) anomalies in 2012 relative to the baseline of 2008–2010. (B) Anomalies of NEP (g C m^{-2} mo^{-1}) in 2012 relative to the mean baseline; numbers atop denote the seasonal anomalies (g C m^{-2}) and their uncertainties, which were derived from Monte-Carlo simulations of monthly fluxes (also shading in A). (C) Anomalies of monthly precipitation (mm mo^{-1}) in 2012 relative to baseline; numbers atop show seasonal anomalies (Wolf et al., 2016).

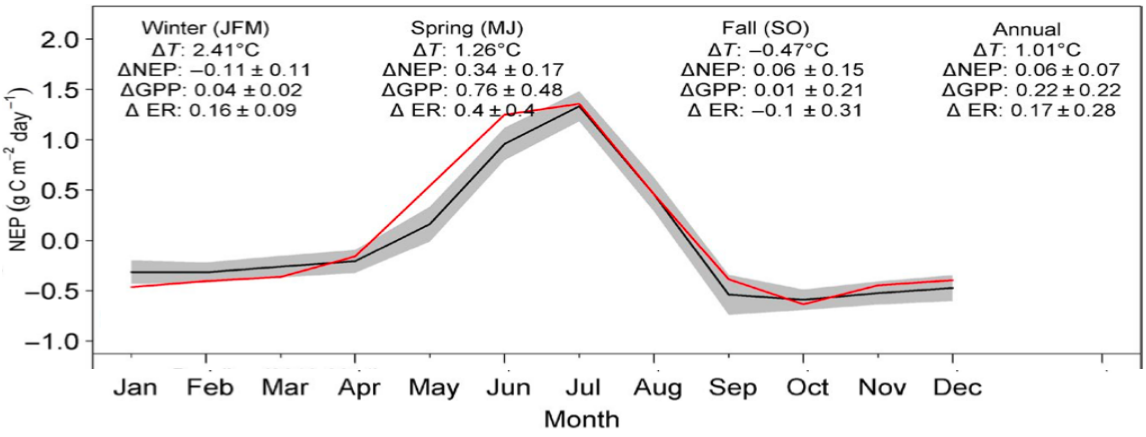

Figure A6. Site-level comparison in NEP using ensemble inversed model simulations (between baseline years (2010–2014; black) and warm spring years (2016; red). Shading denotes 1 *SD* from the 11 inverse model locations. Positive (negative) values indicate land as a carbon sink (source) (Liu et al., 2019).

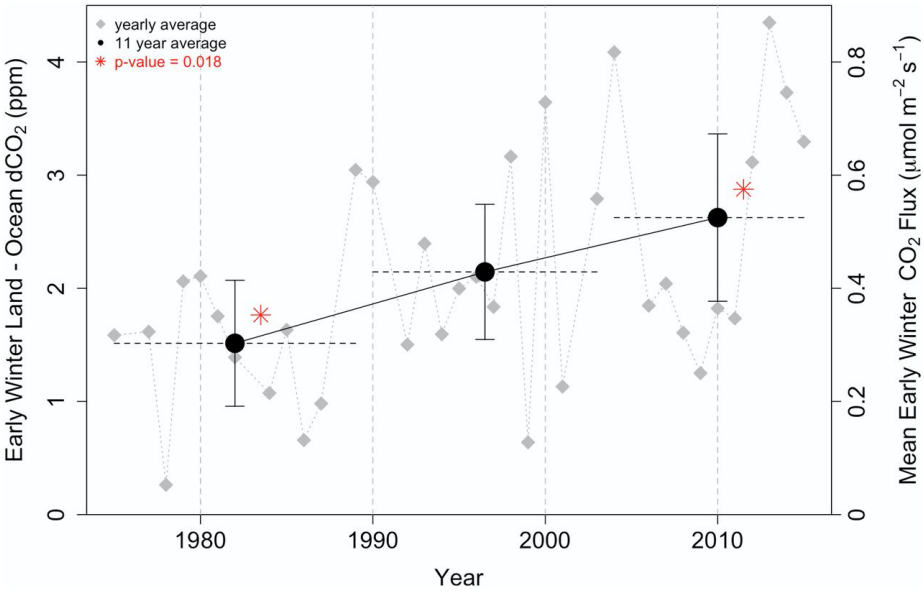

Figure A7. Early winter (October through January CO_2 fluxed measured at the NOAA BRW tower in Barrow, AK, since 1975. The tower is influenced by a large area of the North Slope. The early winter land sector CO_2 has increased by 73.4% ± 10.8% at BRW over 41 y [1.51 ± 0.64 ppm in 1975–1989 to 2.62 ± 0.85 ppm in 2004–2015, a statistically significant increase with P value 0.018, indicated by red asterisks (*)]. Shown are the yearly averaged data (grey diamonds) and 11-year average (black circles) with 95% confidence intervals (error bars) and dashed lines to indicate the years sampled (Commane et al., 2017).

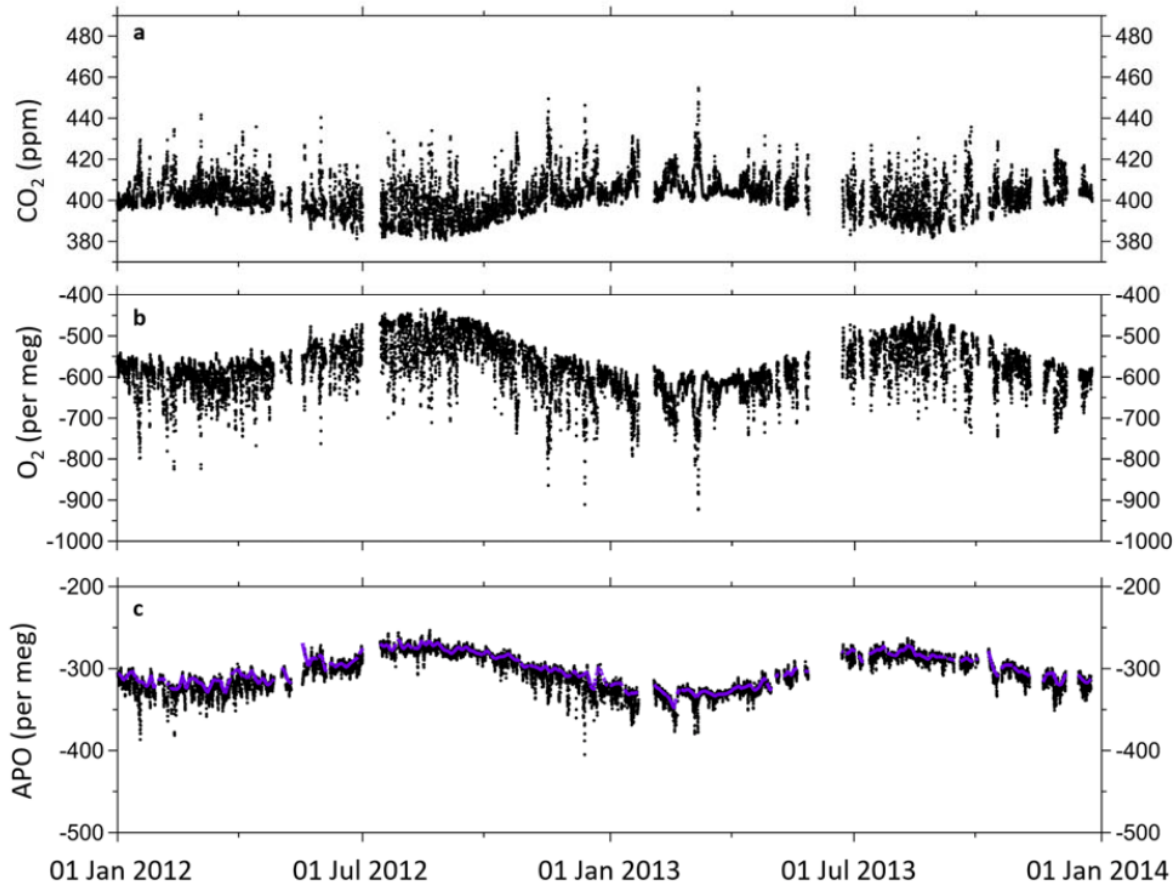

Figure A8. Hourly timeseries of atmospheric CO_2, O_2, and APO observation from WAO (Pickers, 2020). a, Atmospheric CO_2 in ppm. b, Atmospheric O_2, give in 'per meg' units. c, APO, also in per meg units. The purple line in c is the statistically determined 'background', i.e. the APO_{bg} term in Equation 2. $ffCO_2$ is calculated from APO by removing this background signal from the APO observations and dividing by R_{APO} in Equation 2. Each panel shows seasonality that is driven mostly by terrestrial biospheric processes (CO_2 and O_2) and oceanic processes (O_2 and APO). Shorter term variability is driven by diurnal processes, changes in meteorological condition, synoptic-scale variability, and fossil fuel CO_2 emissions (Pickers, et al. 2020).

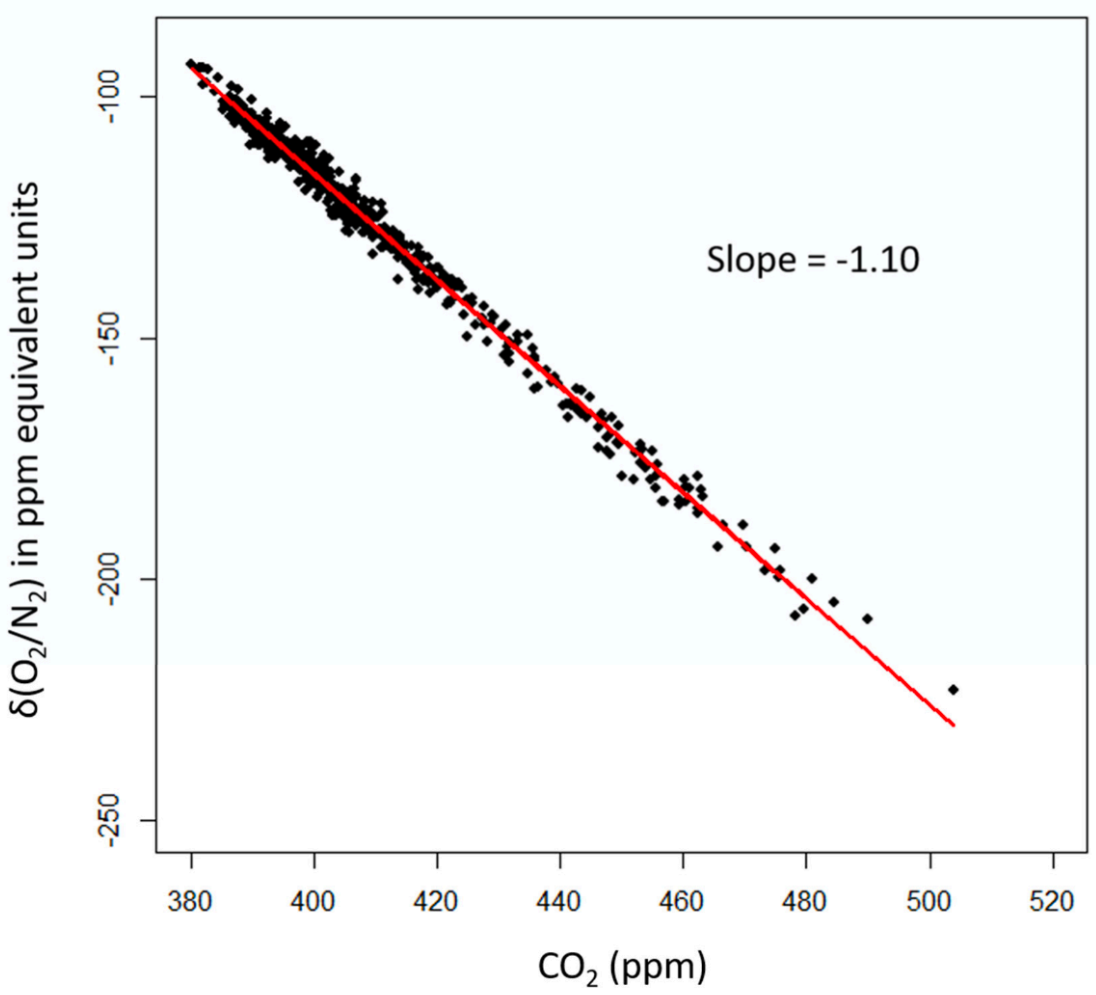

Figure A9. O_2:CO_2 ratio of hourly data measured at UEA. $\delta(O_2/N_2)$ is given in ppm equivalent units to be comparable to CO_2 on a mole per mole basis. The solid red line indicates with a slope of -1.10 indicates that the two species are anti-correlated (Pickers, 2020).

7.2. Appendix B: Additional results from this study.

Table B1. The seven synoptic scale weather type classifications (WTC) used in this study

Cluster	Decoded cluster
1	Strong northerly flow from the North Sea
2	Local north-westerly flow from North Ireland
3	Strong southernly flow from the English Channel
4	Very strong south-westerly flow from the Celtic Sea
5	South-easterly flow from Belgium
6	Very strong westerly flow from Atlantic Ocean
7	North-easterly flow from Denmark

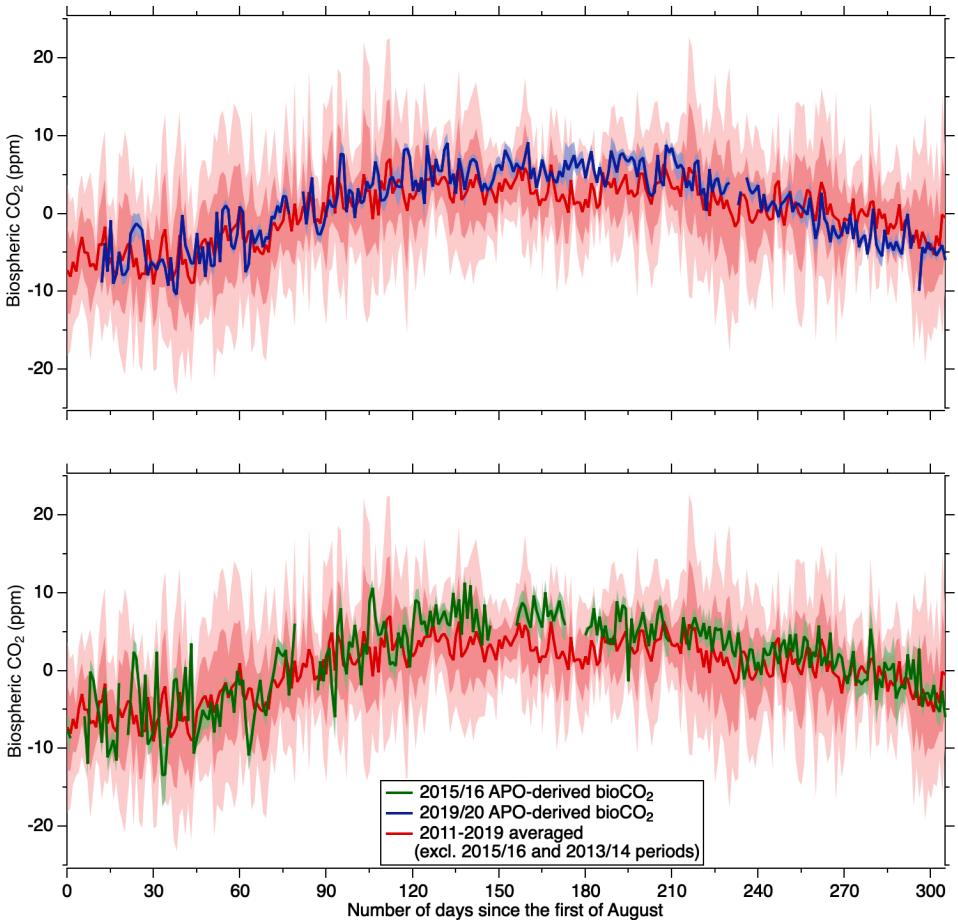

Figure B1. Daily APO-derived biospheric CO_2 concentration (in ppm) at WAO for periods running from the beginning of August to the end of May. The 2015/16 period is shown in green line, the 2019/20 in blue line and baseline mean (01/08/2011-31/07/2019 excluding the 01/08/2015-31/07/2016 and 01/08/2013-31/07/2014 periods) is red line. The green and blue shadings are monthly uncertainty estimates of ffCO_2[APO] at WAO for the 2015/16 and 2019/20 periods respectively; dark red shading and light red shading are respectively 1σ and

2σ away from the monthly mean value. The data has been normalised by subtracting the 12-month mean value from the bioCO_2[APO] data (negative values indicate net CO_2 uptake by the regional terrestrial biosphere and vice versa).

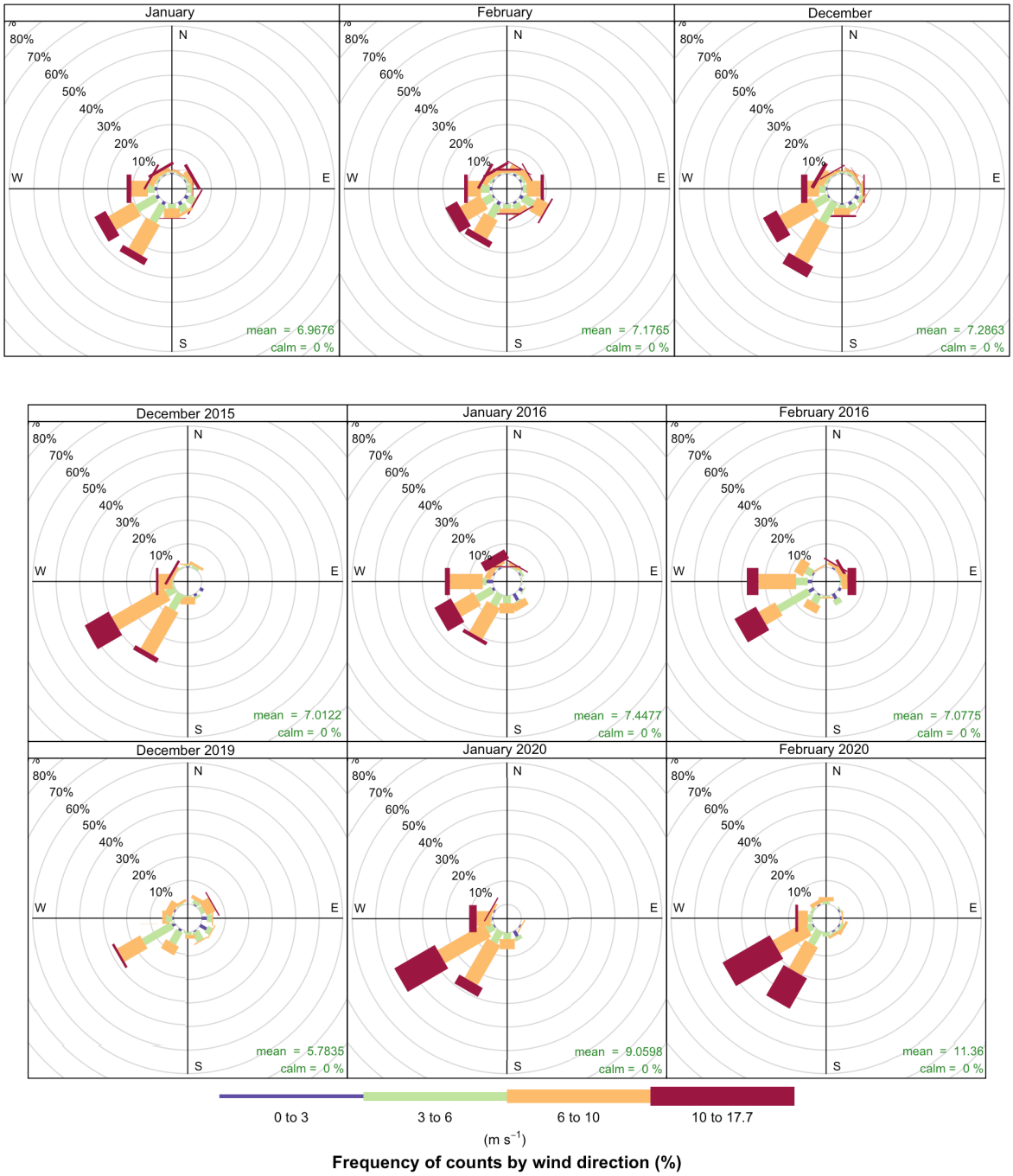

Figure B2. Night-time (01-05 UTC) wind rose of each month in the December-February period at WAO. a, the 2011-19 period excluding the 2015/16 period; b, the 2015/16 period; c, the 2019/20 period.

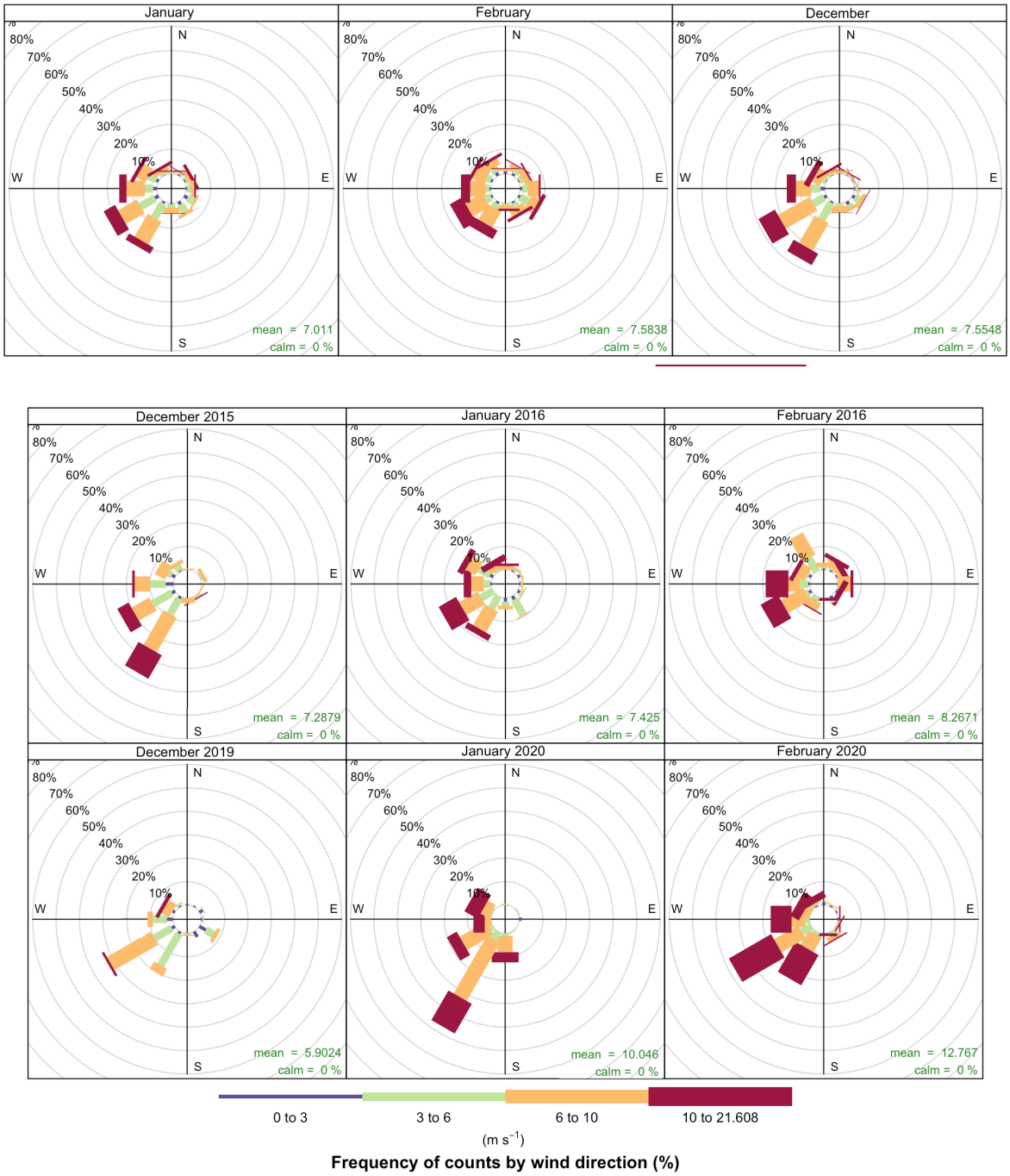

Figure B3. Day-time (11-15 UTC) wind rose of each month in the December-February period at WAO. a, the 2011-19 period excluding 2015/16 period; b, the 2015/16 period; c, the 2019/20 period.

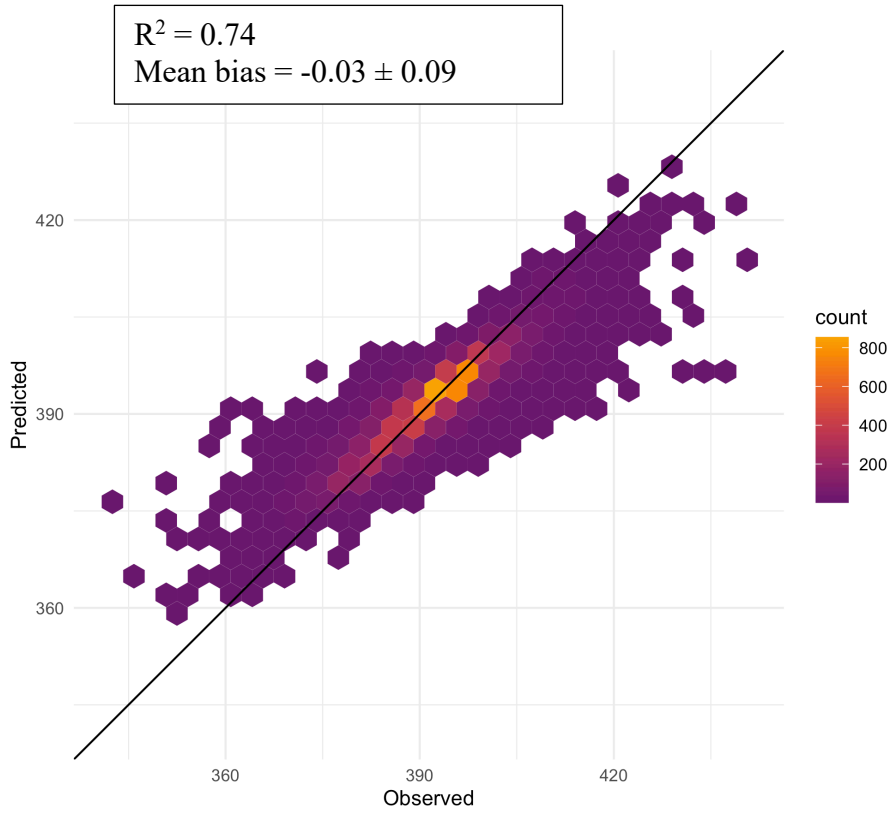

Figure B4. Scatter plot of observed and modelled bioCO_2 from the trained Random Forest model algorithm. The plot is made using data from the model test set only, which are withheld from model training. The black line represents a 1:1 relationship. Observed bioCO_2 is calculated using the APO approach (see Method). The mean bias is calculated from daily observed-modelled bioCO_2 differences.

7.3. Appendix C: Eliminating the anthropogenic trend associated with O_2 and CO_2 measurements

There is a continuing increase of atmospheric CO_2 content is caused by anthropogenic CO_2 emissions – most importantly fossil fuel burning. At the same time, atmospheric O_2 is declining at a rate comparable with fossil fuel emissions of CO_2 (combustion consumes O_2). Analysing the CO_2 and O_2 data sets often benefits by including consideration of plots of detrended data. This section outlines a simple method for accomplishing the calculations and creation of a plot of detrended data. Rather than just describing the general techniques, this section provides a step by step look at the components of a spread sheet where the CO_2 timeseries is detrended. The long term decreasing trend in O_2 data will be eliminated similarly.

The first step in creating a detrended time series is to calculate the **overall trend of the data**. This can be done on the plot by including a linear fit to the data or by using the Excel SLOPE function (Figure C1). Once the data points that represent the time series trend are calculated (Figure C2), the difference between individual data points and the trend can be calculated to **produce residual values** (Figure C3). Figure C4 shows the data before and after detrend the data.

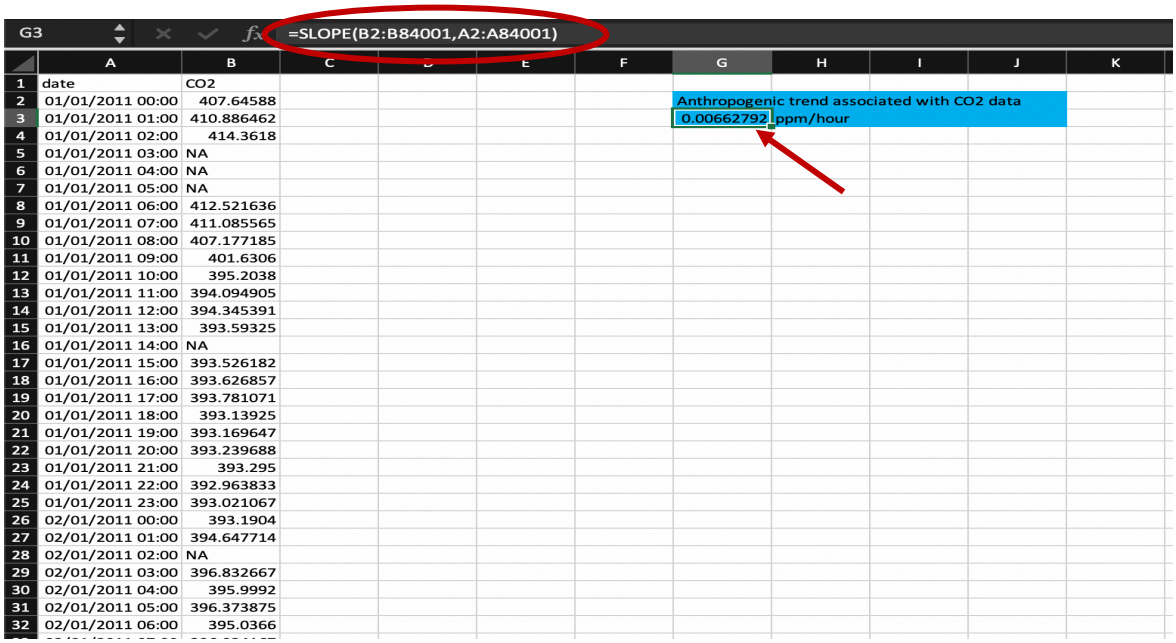

	A	B
1	date	CO2
2	01/01/2011 00:00	407.64588
3	01/01/2011 01:00	410.886462
4	01/01/2011 02:00	414.3618
5	01/01/2011 03:00	NA
6	01/01/2011 04:00	NA
7	01/01/2011 05:00	NA
8	01/01/2011 06:00	412.521636
9	01/01/2011 07:00	411.085565
10	01/01/2011 08:00	407.177185
11	01/01/2011 09:00	401.6306
12	01/01/2011 10:00	395.2038
13	01/01/2011 11:00	394.094905
14	01/01/2011 12:00	394.345391
15	01/01/2011 13:00	393.59325
16	01/01/2011 14:00	NA
17	01/01/2011 15:00	393.526182
18	01/01/2011 16:00	393.626857
19	01/01/2011 17:00	393.781071
20	01/01/2011 18:00	393.13925
21	01/01/2011 19:00	393.169647
22	01/01/2011 20:00	393.239688
23	01/01/2011 21:00	393.295
24	01/01/2011 22:00	392.963833
25	01/01/2011 23:00	393.021067
26	02/01/2011 00:00	393.1904
27	02/01/2011 01:00	394.647714
28	02/01/2011 02:00	NA
29	02/01/2011 03:00	396.832667
30	02/01/2011 04:00	395.9992
31	02/01/2011 05:00	396.373875
32	02/01/2011 06:00	395.0366

Figure C1. Use of the SLOPE function to calculate linear trend of the CO_2 time series.

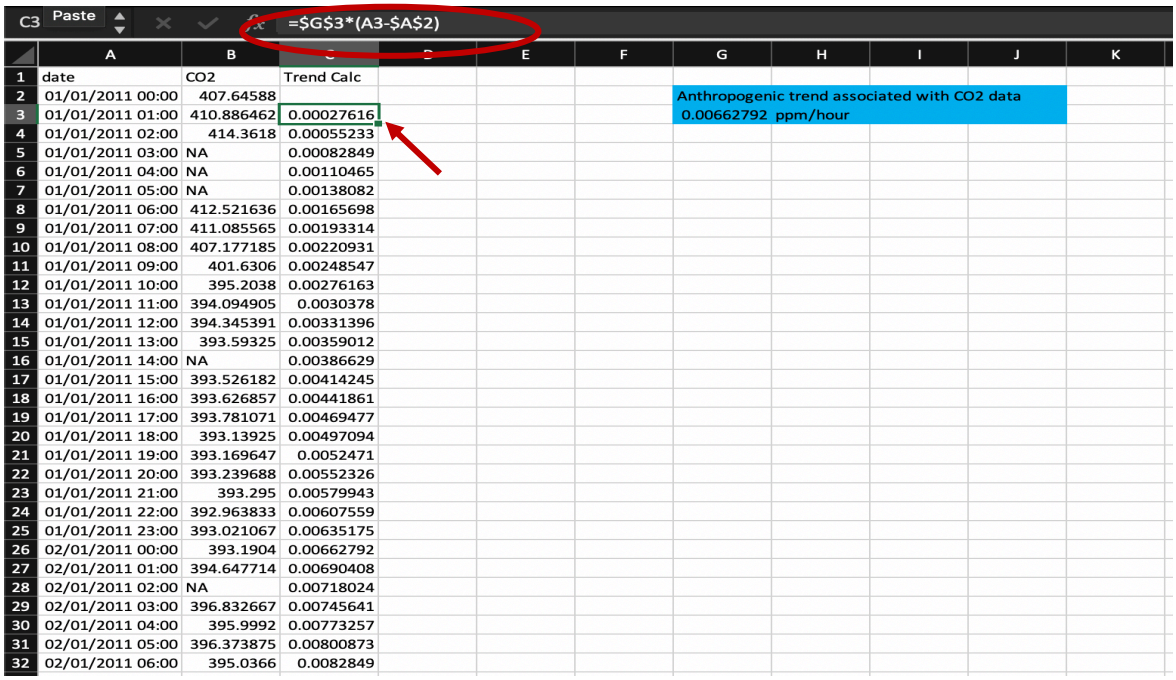

	A	B	C	D	E	F	G	H	I	J	K
1	date	CO2	Trend Calc								
2	01/01/2011 00:00	407.64588									
3	01/01/2011 01:00	410.886462	0.00027616								
4	01/01/2011 02:00	414.3618	0.00055233								
5	01/01/2011 03:00	NA	0.00082849								
6	01/01/2011 04:00	NA	0.00110465								
7	01/01/2011 05:00	NA	0.00138082								
8	01/01/2011 06:00	412.521636	0.00165698								
9	01/01/2011 07:00	411.085565	0.00193314								
10	01/01/2011 08:00	407.177185	0.00220931								
11	01/01/2011 09:00	401.6306	0.00248547								
12	01/01/2011 10:00	395.2038	0.00276163								
13	01/01/2011 11:00	394.094905	0.0030378								
14	01/01/2011 12:00	394.345391	0.00331396								
15	01/01/2011 13:00	393.59325	0.00359012								
16	01/01/2011 14:00	NA	0.00386629								
17	01/01/2011 15:00	393.526182	0.00414245								
18	01/01/2011 16:00	393.626857	0.00441861								
19	01/01/2011 17:00	393.781071	0.00469477								
20	01/01/2011 18:00	393.13925	0.00497094								
21	01/01/2011 19:00	393.169647	0.0052471								
22	01/01/2011 20:00	393.239688	0.00552326								
23	01/01/2011 21:00	393.295	0.00579943								
24	01/01/2011 22:00	392.963833	0.00607559								
25	01/01/2011 23:00	393.021067	0.00635175								
26	02/01/2011 00:00	393.1904	0.00662792								
27	02/01/2011 01:00	394.647714	0.00690408								
28	02/01/2011 02:00	NA	0.00718024								
29	02/01/2011 03:00	396.832667	0.00745641								
30	02/01/2011 04:00	395.9992	0.00773257								
31	02/01/2011 05:00	396.373875	0.00800873								
32	02/01/2011 06:00	395.0366	0.0082849								

Figure C2. Calculation of the daily values for daily increment of trend.

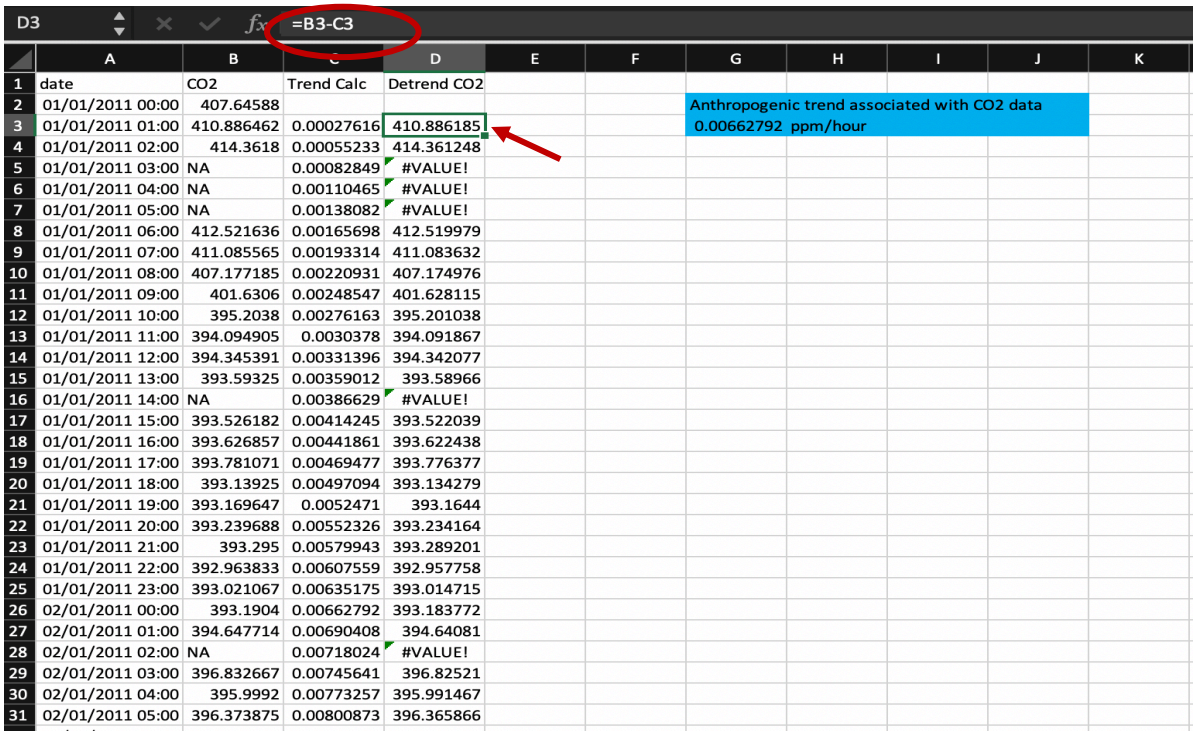

	A	B	C	D	E	F	G	H	I	J	K
1	date	CO2	Trend Calc	Detrend CO2							
2	01/01/2011 00:00	407.64588									
3	01/01/2011 01:00	410.886462	0.00027616	410.886185							
4	01/01/2011 02:00	414.3618	0.00055233	414.361248							
5	01/01/2011 03:00	NA	0.00082849	#VALUE!							
6	01/01/2011 04:00	NA	0.00110465	#VALUE!							
7	01/01/2011 05:00	NA	0.00138082	#VALUE!							
8	01/01/2011 06:00	412.521636	0.00165698	412.519979							
9	01/01/2011 07:00	411.085565	0.00193314	411.083632							
10	01/01/2011 08:00	407.177185	0.00220931	407.174976							
11	01/01/2011 09:00	401.6306	0.00248547	401.628115							
12	01/01/2011 10:00	395.2038	0.00276163	395.201038							
13	01/01/2011 11:00	394.094905	0.0030378	394.091867							
14	01/01/2011 12:00	394.345391	0.00331396	394.342077							
15	01/01/2011 13:00	393.59325	0.00359012	393.58966							
16	01/01/2011 14:00	NA	0.00386629	#VALUE!							
17	01/01/2011 15:00	393.526182	0.00414245	393.522039							
18	01/01/2011 16:00	393.626857	0.00441861	393.622438							
19	01/01/2011 17:00	393.781071	0.00469477	393.776377							
20	01/01/2011 18:00	393.13925	0.00497094	393.134279							
21	01/01/2011 19:00	393.169647	0.0052471	393.1644							
22	01/01/2011 20:00	393.239688	0.00552326	393.234164							
23	01/01/2011 21:00	393.295	0.00579943	393.289201							
24	01/01/2011 22:00	392.963833	0.00607559	392.957758							
25	01/01/2011 23:00	393.021067	0.00635175	393.014715							
26	02/01/2011 00:00	393.1904	0.00662792	393.183772							
27	02/01/2011 01:00	394.647714	0.00690408	394.64081							
28	02/01/2011 02:00	NA	0.00718024	#VALUE!							
29	02/01/2011 03:00	396.832667	0.00745641	396.82521							
30	02/01/2011 04:00	395.9992	0.00773257	395.991467							
31	02/01/2011 05:00	396.373875	0.00800873	396.365866							

Figure C3. Calculation of the residual values (detrend data) for the time series.

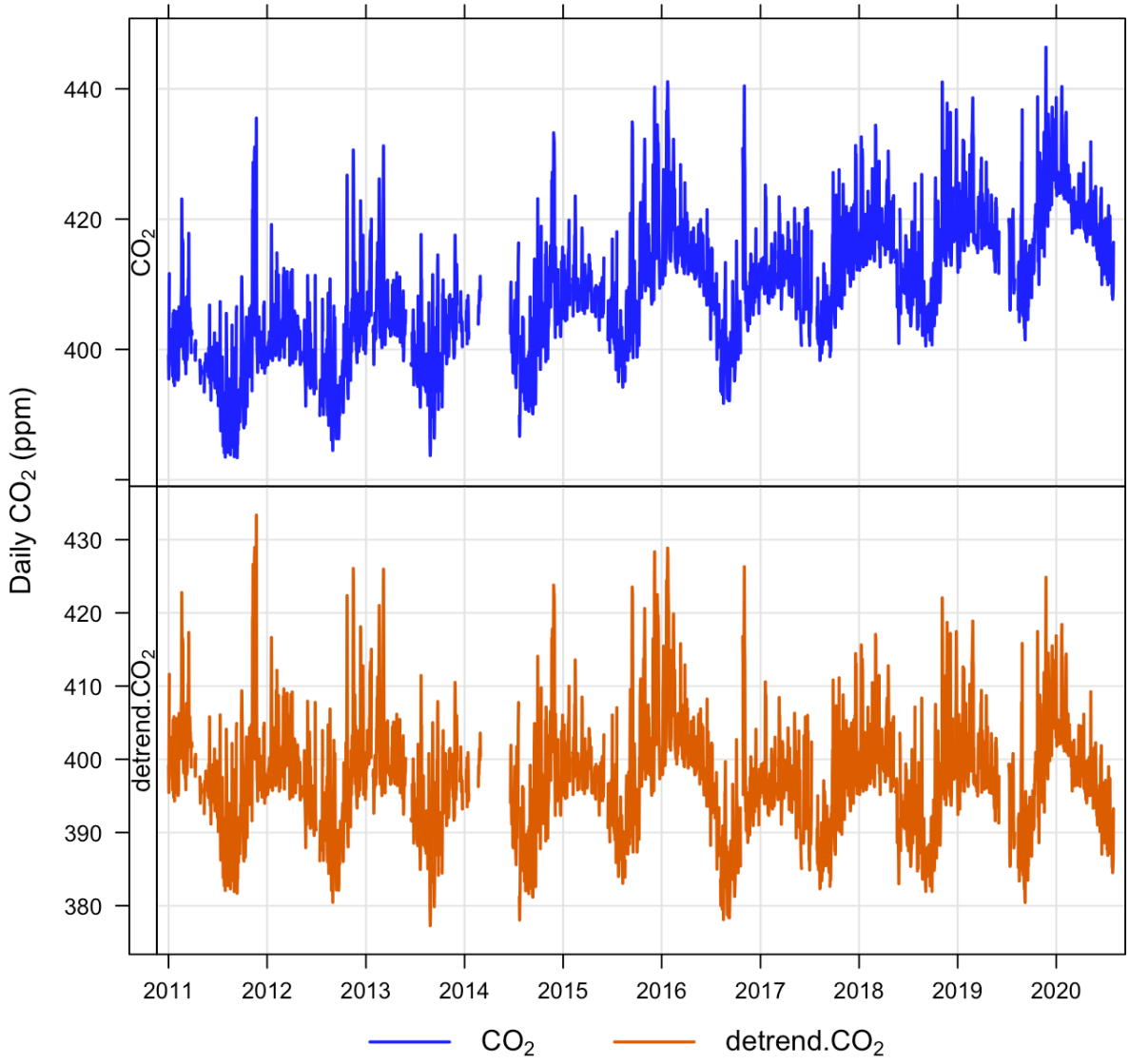

Figure C4. Daily CO_2 (in ppm) data before (top panel) and after (lower panel) eliminating the long term increasing trend associated with anthropogenic processes.